

Optimization Algorithm for Determining the Source Surface Radius Based on Parker Solar Probe in situ Measurements from Encounters 1 to 19

Shiouhe Wang^{1,2}, Fang Shen^{*1,2}, Yi Yang^{1,2}, Xueshang Feng^{1,4}, Jiansen He³

¹SIGMA Weather Group, State Key Laboratory of Solar Activity and Space Weather, National Space Science Center, Chinese Academy of Sciences, Beijing 100190, People's Republic of China

²College of Earth and Planetary Sciences, University of Chinese Academy of Sciences, Beijing 100049, People's Republic of China

³School of Earth and Space Sciences, Peking University, 100871 Beijing, People's Republic of China

⁴Shenzhen Key Laboratory of Numerical Prediction for Space Storm, School of Aerospace, Harbin Institute of Technology, Shenzhen 518055, People's Republic of China

Key Points:

- We prove the well-posedness for PFSS extrapolation and show its inverse problem admits a global minimum via compactness and continuity.
- We construct an optimization algorithm to estimate R_{ss} from comparisons between PFSS extrapolation and PSP in situ measurements.
- ACE validation and Pareto analysis show the optimal R_{ss} generally increases with solar activity while balancing open flux and polarity.

Corresponding author: Fang Shen, fshen@spaceweather.ac.cn

Abstract

The Potential Field Source Surface (PFSS) extrapolation is a method for estimating the large scale coronal magnetic field from photospheric magnetograms. The source surface serves as the outer boundary of its solution domain, and is typically a spherical surface. An appropriate source surface radius (R_{ss}) enables more accurate identification of the coronal magnetic field topology and estimation of the open flux, thereby potentially enhancing the accuracy of space weather modeling. We prove the well-posedness of the PFSS forward problem and establish the existence and uniqueness of the optimal source surface by combining compactness of the admissible set with continuity of the objective functional. The objective functional is the mean squared error (MSE) between PFSS extrapolation and Parker Solar Probe (PSP) radial magnetic field measurements after Parker spiral backmapping and radial scaling for Encounters 1-19. The optimization algorithm is validated with an analytical solution, and Advanced Composition Explorer (ACE) in situ measurements are used as an independent cross-validation dataset. Additional evaluation metrics and Pareto analysis are used to identify the dominant metrics between open flux and polarity prediction accuracy. Our results show that the optimal R_{ss} derived from the algorithm generally increase from solar minimum into the ascending phase of solar cycle 25. The optimized solution improves open flux agreement while preserving or improving polarity prediction accuracy relative to $2.5R_s$. The Pareto frontiers show a transition for dominant metrics from open flux during solar minimum to polarity prediction accuracy during the ascending phase.

Plain Language Summary

The Potential Field Source Surface extrapolation estimates the Sun's large scale coronal magnetic field from photospheric magnetic maps. Its geometry parameter R_{ss} is the source surface radius, and affects which magnetic field lines are open to the heliosphere and how the interplanetary magnetic field in situ measurements backmaps to the solar surface or low corona. In the present study, we use radial magnetic field and solar wind velocity from Parker Solar Probe (PSP) measurements to construct an optimization algorithm to identify which R_{ss} parameter is the optimal value relative to the observations. We then compare the optimal R_{ss} derived from the algorithm and its trend with independent Advanced Composition Explorer (ACE) in situ measurements near 1 Astronomical Unit. The optimal R_{ss} generally increases from solar minimum into the ascending phase of solar cycle 25. The optimized solution improves agreement with open flux calculations while preserving or improving the predicted magnetic field polarity compared to the conventional $2.5R_s$, which helps clarify how to choose R_{ss} under different solar activity cycles.

1 Introduction

The Potential Field Source Surface (PFSS) extrapolation estimates the large scale coronal magnetic field from a photospheric magnetogram by solving Laplace equation for the magnetic scalar potential in the domain between the photosphere and a prescribed source surface. In this extrapolation, the source surface serves as the outer geometric boundary, where the coronal magnetic field is assumed to become radial. The source surface radius (R_{ss}) can influence the modeled distribution of open and closed magnetic field lines, the estimated open magnetic flux, and the candidate solar source regions in-

ferred from backmapping interplanetary in situ measurements. Schatten et al. (1969) estimates R_{ss} at 1.6 solar radius (R_s) by comparing PFSS extrapolations with interplanetary observations. Altschuler and Newkirk (1969) suggests $R_{ss} = 2.5R_s$ by comparing magnetic field line structures from PFSS extrapolations with white light coronal images during the ascending phase of the solar cycle. Subsequent analyses of heliospheric current sheet (HCS) topology and interplanetary magnetic field (IMF) polarity also suggest $R_{ss} = 2.5R_s$ (Hoeksema et al., 1983). The value $R_{ss} = 2.5R_s$ has therefore become a conventional reference choice in PFSS extrapolation studies, with applications to estimating the flux tube expansion factor in the Wang-Sheeley-Argé (WSA) model (Arge et al., 2003; Poduval & Zhao, 2004; Shen et al., 2012; Yalim et al., 2017; Y. Liu et al., 2019; Dakeyo, Rouillard, et al., 2024), initializing coronal magnetohydrodynamic (MHD) simulations (Shen et al., 2007, 2010; Shen, Feng, Wang, et al., 2011; Shen, Feng, Wu, et al., 2011; Shen et al., 2018), studying solar energetic particle transport (L. Zhao & Zhang, 2018; Wei et al., 2019; Zhu & Shen, 2024; Park et al., 2024), and evaluating coronal and heliospheric magnetic field models with observations (Lowder et al., 2014; Hayashi et al., 2016; I. O. I. Virtanen et al., 2022). J. Zhao et al. (2025) uses $R_{ss} = 2.5R_s$ in a statistical analysis of IMF evolution over heliocentric distances from 0.1 to 30 astronomical units (AU).

Despite its widespread applications, $R_{ss} = 2.5R_s$ can lead to discrepancies in the modeled extent of coronal holes and the estimation of the open magnetic flux, indicating that R_{ss} is a tunable parameter and the optimal R_{ss} need be determined by observational constraints. For instance, Lee et al. (2011) analyzes the extent of coronal holes during the minimum phases of solar cycles 22 and 23 to estimate the optimal $R_{ss} = 1.9R_s$ and $1.8R_s$, respectively. Arden et al. (2014) compares the modeled open flux with observations near 1 AU and shows that a larger R_{ss} is required during the maximum phase of solar cycle 23. A lower R_{ss} ($1.5R_s \sim 2.0R_s$) is identified during the solar cycle 24 through comparisons between PFSS extrapolations and IMF measurements near 1 AU (Nikolic, 2019). Total Solar Eclipse (TSE) white light images serve as an essential observable source for coronal magnetic field structures and are used to identify the optimal R_{ss} (Boe et al., 2020; Habbal et al., 2021). Benavitz et al. (2024) analyzes the coronal magnetic field topology during the solar cycle 24 maximum and minimum phases using TSE images, suggesting that the optimal R_{ss} is approximately $1.3R_s$ during the maximum phase of solar cycle and $3.0R_s$ during the minimum phase. Huang et al. (2024) compares the extent of open magnetic field regions in PFSS and MHD models and concludes that R_{ss} increases with solar activity. Further constraints from PFSS extrapolations and in situ measurements also point to a broad range of R_{ss} spanning $1.3R_s$ to $3.5R_s$ (J. S. Koskela et al., 2018; J. Koskela et al., 2019; I. Virtanen & Mursula, 2019; Asvestari et al., 2019; Li et al., 2021; Finley & Brun, 2023; Tähtinen et al., 2024).

Parker Solar Probe (PSP) completed its first encounter during the minimum phase of solar cycle 25 and has since become the closest spacecraft to the Sun to date (Fox et al., 2016; Raouafi et al., 2023). PSP provides an unprecedented opportunity to constrain R_{ss} through comparisons between PFSS extrapolations and in situ measurements near $10R_s$. PFSS extrapolation is commonly used to trace the source regions of solar wind because its computational efficiency and high spatial resolution makes repeated magnetic field lines tracing practical (Schrijver et al., 2006; Badman et al., 2020). The source region mapping is traced through a two-step procedure. The spacecraft position is first ballistically mapped back to source surface footpoints along Parker spiral trajectory using the radial solar wind velocity of in situ measurements (Parker, 1958; Nolte & Roelof,

1973). Magnetic field lines from the PFSS extrapolation are then traced from these foot-points to the photosphere or low corona. Several studies using PSP in situ measurements have shown that the candidate solar source regions inferred by ballistic backmapping and subsequent magnetic field tracing with PFSS extrapolations can vary substantially with the adopted R_{ss} (Dakeyo, Badman, et al., 2024; Koukras et al., 2025; Bizien et al., 2025). For slowly Alfvénic solar wind observed during PSP Encounters 4-14, the foot-point locations of solar wind are found to be most sensitive to the adopted R_{ss} (Ervin et al., 2024). In a source region analysis of slow Alfvénic solar wind observed near low latitudes, a two-step ballistic backmapping method with $R_{ss} = 2.0R_s$ was used to trace the large scale magnetic structure of the solar wind (Bale et al., 2019). Badman et al. (2020) suggests that using a lower R_{ss} ($1.3R_s \sim 1.5R_s$) improves polarity inversion predictions based on PSP in situ measurements during Encounter 1. de Pablos et al. (2022) adopts $R_{ss} = 2.0R_s$ to trace the source regions of polarity inversions during PSP Encounter 1. Bercic et al. (2020) uses this backmapping procedure with $R_{ss} = 2.0R_s$ and indicates coronal electron temperatures consistent with Strahl electron observations from PSP and Helios in the inner heliosphere. Hou et al. (2024) traces switchbacks observed from PSP Encounter 4 back to candidate solar source regions by using a two-step ballistic backmapping procedure with $R_{ss} = 2.0R_s$, and suggests that these switchbacks originate from magnetic reconnection at chromospheric network boundaries.

In summary, previous studies suggest that no single R_{ss} is universally preferred. Badman et al. (2022) shows that PFSS extrapolations do not generally yield a single globally optimal R_{ss} when coronal hole distribution, streamer belt topology, and magnetic polarity are evaluated simultaneously. This result suggests that the preferred R_{ss} depends on which observational constraints and evaluation metrics are emphasized. To characterize such trade-offs, we use a Pareto analysis, in which a solution is regarded as Pareto optimal if no objective can be improved without degrading at least one other objective (Miettinen, 1999; Deb, 2001; Chang, 2015). It remains unclear whether the optimization of R_{ss} exhibits a well-defined Pareto frontier among competing evaluation metrics, and how the optimal R_{ss} varies with solar activity for a prescribed objective functional.

Previous studies have explored nonspherical source surface as a way to improve the agreement between coronal magnetic field extrapolations and observations (Schulz et al., 1978; Levine et al., 1982; Schulz, 1997; Panasenco et al., 2020; Kruse et al., 2020, 2021). Figure 1(a) shows the spherical reference geometry, and Figure 1(b) shows a nonspherical geometry with the same inner fixed boundary but an outer free boundary. For a prescribed outer boundary, such nonspherical boundary value problems can be solved numerically, for example by finite element methods (FEMs) (Kang & Zhong-Ci, 1996). In many practical applications, the source surface geometry is not known a priori. Some studies have considered prescribed nonspherical geometries, such as an elliptic outer boundary (Kruse et al., 2020, 2021). This geometry in advance would introduce an artificial restriction on the coronal field topology. If additional observational condition is imposed on the outer boundary, the resulting boundary conditions will become overdetermined for a fixed domain. The natural mathematical formulation is then a free boundary or shape optimization problem, in which the magnetic field and the outer boundary geometry need be determined simultaneously. Shape optimization provides a rigorous framework for this problem by minimizing a prescribed objective functional over an admissible class of domains (Sokolowski & Zolesio, 1992). This motivates a standardized shape optimization formulation for nonspherical coronal magnetic field extrapolations.

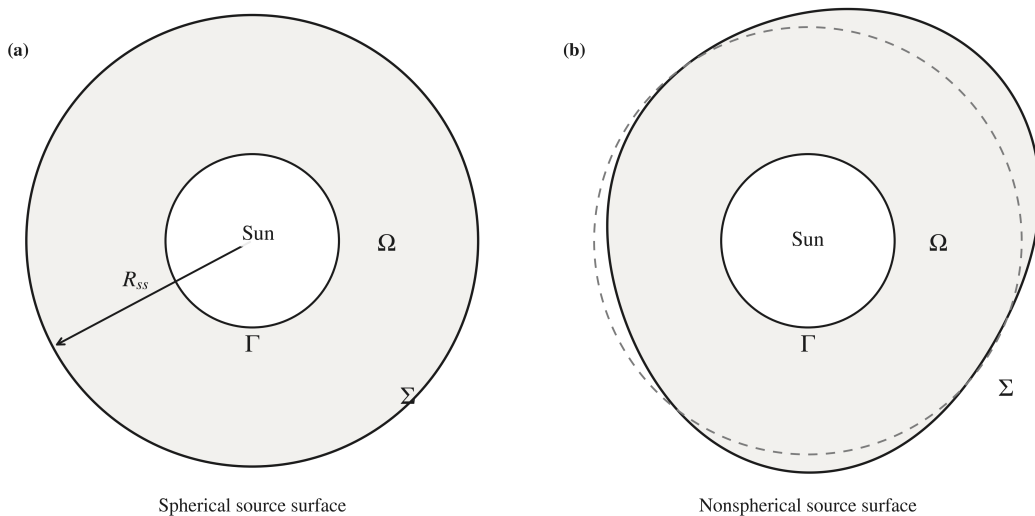


Figure 1: (a) Illustration of the solution domain for PFSS extrapolation with a spherical source surface of radius R_{ss} . (b) Illustration of the solution domain for PFSS extrapolation with a nonspherical source surface, where Ω denotes the solution domain, Γ denotes the inner fixed boundary, and Σ denotes the outer free boundary.

Section 2 establishes the well-posedness of the forward PFSS problem and formulates the estimation of R_{ss} within a free boundary framework. We then prove the compactness of the admissible class and the continuity of the objective functional, which together imply the existence of a global minimum for this inverse problem. These arguments apply directly to nonspherical source surface geometries, and are not restricted to the spherical case. Section 3 describes the magnetogram, PSP, and ACE datasets and clarifies how to integrate the PFSS extrapolation, Parker spiral backmapping, and cross-validation with these observations. Section 4 defines the objective functional, constructs the optimization algorithm and its validation, and introduces the additional evaluation metrics and Pareto analysis. Section 5 shows the optimal values of R_{ss} for PSP Encounters 1-19, examines how R_{ss} vary with solar activity, and analyzes the results using the evaluation metrics and Pareto frontiers. Section 6 concludes the paper.

2 Mathematical Formulation

In this section, we formulate the source surface inverse problem as a free boundary problem. The formulation applies to both spherical and nonspherical source surfaces. We first prove the well-posedness of the forward problem for PFSS extrapolation and then prove the existence and uniqueness of a minimizer for the associated free boundary optimization problem. For the forward problem, the well-posedness means the existence and uniqueness of the PDE solution ψ for a prescribed domain. For the inverse problem, we need to establish the existence and uniqueness of a source surface geometry of minimizing

the objective functional over the admissible set. The compactness and continuity of the admissible set and the objective functional need to be established. These arguments in this section can apply directly to nonspherical source surface geometries, not only to the spherical case used later in the optimization algorithm.

2.1 Description

The forward problem for PFSS extrapolation is a second order elliptic boundary value problem with mixed boundary conditions and therefore belongs to a class of steady state problems. If both its solution and the outer boundary need to be determined from additional boundary conditions or observational constraints, the problem is formulated as a free boundary problem (Tepper, 1975; Acker, 1981). Due to the internal Neumann boundary condition for PFSS extrapolation in the forward problem, existing research results for free boundary problems cannot be applied directly, so the proof must be rebuilt for the setting of the PFSS extrapolation.

We first introduce the functional definitions used in the variational formulation for the free boundary problem. Since the equation underlying the PFSS extrapolation is an elliptic boundary value problem for the scalar potential ψ , and the magnetic field is given by $\mathbf{B} = -\nabla\psi$, the natural energy space is $H^1(\Omega)$. This space requires only square integrable weak derivatives, gives finite magnetic energy $\int_{\Omega} |\nabla\psi|^2 dx$, and provides well-defined boundary traces for imposing Dirichlet and Neumann conditions. More mathematical foundations of Sobolev spaces and elliptic PDEs can be found in classical references (Strauss, 2008; Evans, 2010).

Let $m \in \mathbb{N}$ and $p \in [1, \infty]$. The Sobolev space $W^{m,p}(\Omega)$ is defined as

$$W^{m,p}(\Omega) := \{u \in L^p(\Omega) \mid \partial^\alpha u \in L^p(\Omega), \forall \alpha \in \mathbb{N}^3, |\alpha| \leq m\}, \quad (1)$$

where α is a multi-index and $L^p(\Omega)$ denotes the Lebesgue p -integrable functions space. For $1 \leq p < \infty$, $W^{m,p}(\Omega)$ is equipped with the norm

$$\|u\|_{W^{m,p}(\Omega)} := \left(\sum_{|\alpha| \leq m} \|\partial^\alpha u\|_{L^p(\Omega)}^p \right)^{1/p}. \quad (2)$$

In particular, $W^{m,2}(\Omega)$ is denoted by $H^m(\Omega)$. In this work, the scalar potential in the PFSS extrapolation is sought in $H^1(\Omega)$, which is the standard space for the weak formulation of second order elliptic problems. We next define the admissible set of domains for the free boundary problem.

Definition 1 (The Admissible Set). *Let Ω be the annular domain in \mathbb{R}^3 with the inner fixed boundary Γ and the outer free boundary Σ . Γ and Σ are C^2 -smooth and homeomorphic to the unit sphere. The admissible set \mathcal{A} is*

$$\mathcal{A} := \{\Omega \subset \mathbb{R}^3 \mid \partial\Omega = \Gamma \cup \Sigma, \Gamma \text{ is fixed and } \Sigma \text{ is free, both of class } C^2 \text{ and simply connected}\}. \quad (3)$$

The solution to the free boundary problem consists of finding a domain $\Omega \in \mathcal{A}$ that satisfies the additional boundary conditions, which is imposed on the free boundary Σ . The problem is formally defined as follows.

Definition 2 (Free Boundary Problem). *Let $\Omega \in \mathcal{A}$ be an annular domain, where \mathcal{A} is defined in Definition 1. The free boundary problem consists of finding a domain Ω and a function $\psi \in H^1(\Omega)$ such that*

$$\begin{cases} -\mathcal{L}\psi = 0 & \text{in } \Omega, \\ \partial_{\mathbf{n}}\psi = g & \text{on } \Gamma, \\ \psi = 0 & \text{on } \Sigma, \\ \partial_{\mathbf{n}}\psi = h & \text{on } \Sigma, \end{cases} \quad (4)$$

where \mathcal{L} is the prescribed differential operator and the exterior normal derivative is $\partial_{\mathbf{n}}\psi := \nabla\psi \cdot \mathbf{n}$, with \mathbf{n} denoting the outward unit normal on $\partial\Omega$. The Neumann data are $g \in H^{-\frac{1}{2}}(\Gamma)$ on the inner boundary Γ and $h \in H^{-\frac{1}{2}}(\Sigma)$ on the outer boundary Σ . The Dirichlet condition prescribes zero potential on Σ .

Relevant studies in free boundary problems primarily focus on the external Bernoulli free boundary problem with internal Dirichlet condition (Alt & Schumny, 1984; Ito et al., 2006; Ivanyshyn Yaman & Kress, 2017), originating from the ideal fluid dynamics (Caffarelli & Alt, 1981). Although the existence and uniqueness of the solution for this internal Dirichlet boundary value are well-established (Lieberman, 1986; Rabago & Azegami, 2019), these properties for the internal Neumann condition have not been proven. The free boundary problem for PFSS extrapolation differs from the Bernoulli free boundary problem because it imposes an internal Neumann condition, which is weaker than the internal Dirichlet condition used in the Bernoulli free boundary problem. The well-posedness of the problem need to be rebuilt and can be proven by analyzing the variational equations in the shape optimization framework (Sokolowski & Zolesio, 1992; Kawohl, 2019; Rabago & Azegami, 2019). We apply the shape optimization framework to formulate this free boundary problem.

Definition 3 (Objective Functional). *The objective functional $\mathcal{J}(\Omega)$ is constructed from the two auxiliary problems (5a) and (5b):*

$$\text{find } \Omega \in \mathcal{A} : \begin{cases} \text{find } \psi_D \in H^1(\Omega), \text{ such that:} & \begin{cases} -\Delta\psi_D = 0 & \text{in } \Omega, \\ \partial_{\mathbf{n}}\psi_D = g & \text{on } \Gamma, \\ \psi_D = 0 & \text{on } \Sigma, \end{cases} \end{cases} \quad (5a)$$

$$\begin{cases} \text{find } \psi_R \in H^1(\Omega), \text{ such that:} & \begin{cases} -\Delta\psi_R = 0 & \text{in } \Omega, \\ \partial_{\mathbf{n}}\psi_R = g & \text{on } \Gamma, \\ \partial_{\mathbf{n}}\psi_R + \beta\psi_R = h & \text{on } \Sigma. \end{cases} \end{cases} \quad (5b)$$

where ψ_D and ψ_R are the two auxiliary solutions used to define the objective functional $\mathcal{J}(\Omega)$.

The shape optimization minimizes the functional \mathcal{J} over the admissible domains \mathcal{A} . The well-posedness does not depend on the particular choice of objective functional. In general, the single objective functional used in shape optimization is not unique, while the solution to the free boundary problem is invariant (Rabago & Azegami, 2020). Thus, the optimizer recovers the physically meaningful free boundary.

Definition 4 (Shape Optimization). *The shape optimization is formulated as a single objective optimization problem with PDE constraints.*

$$\begin{cases} \min_{\Omega \in \mathcal{A}} \mathcal{J}(\Omega) = \min_{\Omega \in \mathcal{A}} \int_{\Omega} |\nabla(\psi_D - \psi_R)|^2 dx, \\ F(\mathbf{x}, \psi, \partial_{\mathbf{n}}\psi, \Delta\psi; \Omega) = 0, \end{cases} \quad (6)$$

where F represents the combination of PDE and boundary conditions.

The shape optimization problem is equivalent to the free boundary problem. We use variational calculus to prove the existence and uniqueness of Definition 4. The key is to construct a solution set satisfying the PDE constraints and then study the property of functional \mathcal{J} on this set. If the set is compact and \mathcal{J} is continuous, then \mathcal{J} attains a minimum. Continuity of \mathcal{J} is straightforward; the main difficulty is to establish compactness. We first need to prove the well-posedness of the forward problem for PFSS extrapolation and then analyze the compactness of the solution set. Only the main steps are given here, and the detailed arguments are shown in Appendix C.

2.2 The well-posedness of the forward problem for PFSS extrapolation

The well-posedness of the forward problem for PFSS extrapolation means the existence and uniqueness of the solution ψ . This property is essential both for coronal magnetic field simulations and the free boundary problem. The forward problem for PFSS extrapolation is a mixed Dirichlet and Neumann boundary value problem, and we prove its well-posedness by reformulating it in variational form on the Sobolev space. We first derive the variational equation and identify the corresponding solution space. We then define the associated bilinear form and apply the Lax-Milgram theorem to prove the existence and uniqueness of the solution. The proof is carried out for a general nonspherical source surface, with the spherical case included as a special case.

Lemma 2.1 (Variational Equation of the Forward Problem for PFSS Extrapolation). *A function $\psi \in V(\Omega)$ solves the forward problem for PFSS extrapolation if and only if for any $\phi \in V(\Omega)$,*

$$\int_{\Omega} (\nabla\psi) \cdot (\nabla\phi) dx = \int_{\Gamma} g\gamma_0(\phi) d\sigma, \quad (7)$$

where $V(\Omega) = \{v \in H^1(\Omega) : v|_{\Sigma} = 0\}$ is equipped with the norm $\|\cdot\|_{H^1(\Omega)}$, and γ_0 denotes the trace operator mapping functions to their boundary values.

Proof. *Shown in Appendix C.*

This lemma establishes the equivalence between the forward problem for PFSS extrapolation and its variational formulation. We apply the Lax-Milgram theorem to this variational equation and then yields the well-posedness of the forward problem. We first define the bilinear functional $a(\cdot, \cdot): V \times V \rightarrow \mathbb{R}$ by

$$a(\psi, \phi) := \int_{\Omega} (\nabla\psi) \cdot (\nabla\phi) dx, \quad \forall (\psi, \phi) \in V \times V, \quad (8)$$

and a linear functional $\eta_g: V \rightarrow \mathbb{R}$ by

$$\eta_g(\phi) := \int_{\Gamma} g\gamma_0(\phi) d\sigma, \quad \forall \phi \in V. \quad (9)$$

Then, the variational equation can be represented by these form:

$$(7) \iff \text{Find } \psi \in V, \text{ such that } a(\psi, \phi) = \eta_g(\phi), \quad \forall \phi \in V. \quad (10)$$

If $a(\cdot, \cdot)$ and $\eta_g(\cdot)$ satisfy the assumptions of the Lax-Milgram theorem, then the forward problem for PFSS extrapolation is well-posed. We verify these assumptions in the following theorem.

Theorem 2.1 (Well-posedness of the Forward Problem for PFSS Extrapolation). *The variational equation $a(\psi, \phi) = \eta_g(\phi)$ has a unique solution in V .*

Proof. *Shown in Appendix C.*

The variational formulation for the forward problem extends naturally to the two auxiliary problems (5a) and (5b). Once a convergent sequence of the admissible domain leading to the shape optimization of (6) is constructed, the free boundary problem for PFSS extrapolation is well-posed.

2.3 The well-posedness of the free boundary problem for PFSS extrapolation

We now define the solution space for the free boundary problem and prove its compactness.

Definition 5 (Solution Space). *To solve the optimization problem (6), we define the space of triples*

$$\mathcal{M} := \{(\Omega, \psi_D, \psi_R) : \Omega \in \mathcal{A}; \psi_D, \psi_R \in H^1(\tilde{U}), \text{ and satisfy the (5a) and (5b)}\}, \quad (11)$$

where \tilde{U} is a fixed extension domain containing every admissible domain in \mathcal{A} .

Prior to analyzing the convergence of sequences within \mathcal{M} , a parameterization of Ω is necessary. There exists a diffeomorphism $\varphi : \mathbb{S}^2 \rightarrow \Sigma$ such that φ uniquely determines the outer boundary $\Sigma(\varphi)$, which in turn uniquely determines the admissible domain $\Omega(\Sigma)$. Each element in \mathcal{A} can be characterized by φ . We therefore define the convergence of domains $\Omega_n \rightarrow \Omega$ through the convergence of their parameterizations, $\varphi_n \rightarrow \varphi$. Figure 2(a) shows the geometric setting of the free boundary problem and the admissible variations of the outer boundary Σ . Figure 2(b) summarizes the proof strategy on the fixed extension domain \tilde{U} and shows how the auxiliary solutions (5a) and (5b) enter the compactness and lower semicontinuity that yields a common limit and a minimizer of the objective functional \mathcal{J} . The following result establishes the compactness of \mathcal{M} . This argument extends the Bernoulli free boundary framework to the free boundary problem for PFSS extrapolation and corrects the erroneous of proof given in (Rabago & Azegami, 2019).

Lemma 2.2 (The Compactness of \mathcal{M}). *Let $(\varphi_n, \psi_{D_n}, \psi_{R_n})$ be a sequence in \mathcal{M} , where ψ_{D_n} and ψ_{R_n} are weak solutions of (5a) and (5b) in $\Omega_n = \Omega(\Sigma(\varphi_n))$, respectively. Then, there exists a subsequence $(\varphi_{n_k}, \psi_{D_{n_k}}, \psi_{R_{n_k}})$, a mapping $\varphi \in \mathcal{P}$ and functions $\psi_D, \psi_R \in V(\tilde{U}), H^1(\tilde{U})$, respectively, such that:*

$$\begin{cases} \varphi_{n_k} \rightarrow \varphi & \text{in } \mathcal{P}, \\ \psi_{D_{n_k}} \rightarrow \psi_D & \text{in } V(\tilde{U}), \\ \psi_{R_{n_k}} \rightarrow \psi_R & \text{in } H^1(\tilde{U}), \end{cases} \quad (12)$$

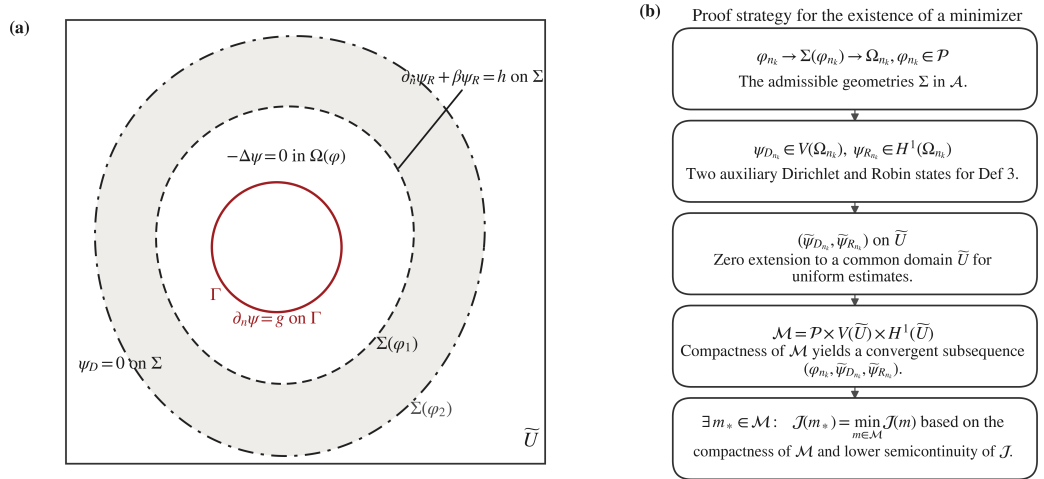


Figure 2: (a) Geometric setting of the free boundary problem for PFSS extrapolation. The two black dashed source surface boundaries represent admissible variations of the outer free boundary, where red boundary Γ denotes the inner fixed boundary and \bar{U} denotes the fixed extension domain. (b) Proof strategy of free boundary problem. The diagram summarizes the passage from admissible geometries and the auxiliary Dirichlet and Robin states to their zero extensions on \bar{U} , followed by the compactness and lower semicontinuity that yields a minimizer of the objective functional \mathcal{J} .

where ψ_D, ψ_R are solutions to (5a) and (5b) restricted to the optimal domain $\Omega(\varphi)$.

Proof. Shown in Appendix C.

The following theorem establishes the existence and uniqueness of a minimum for the optimization problem (6), based on Lemma 2.2.

Theorem 2.2 (Existence and Uniqueness of a Minimum for the Optimization Problem). *The optimization problem (6) admits a unique minimum.*

Proof. *The single objective functional $\mathcal{J}(\Omega, \psi_D(\Omega), \psi_R(\Omega))$ is lower semicontinuous when the boundaries Σ and Γ are C^2 . A continuous functional on a compact set attains its extrema. Therefore, by the compactness of \mathcal{M} and the lower semicontinuity of \mathcal{J} , there exists a subsequence $(\Omega_{n_k}, \psi_{D_{n_k}}, \psi_{R_{n_k}})$ from Lemma 2.2 such that*

$$\lim_{k \rightarrow \infty} \mathcal{J}(\Omega_{n_k}, \psi_{D_{n_k}}, \psi_{R_{n_k}}) = \inf \{ J(\Omega, \psi_D(\Omega), \psi_R(\Omega)) : (\Omega, \psi_D(\Omega), \psi_R(\Omega)) \in \mathcal{M} \}. \quad (13)$$

By Lemma 2.2, the sequence $(\Omega_{n_k}, \psi_{D_{n_k}}, \psi_{R_{n_k}})$ converges to (Ω, ψ_D, ψ_R) , where ψ_D, ψ_R are defined on the optimal domain Ω . ■

We therefore prove the well-posedness of the forward problem for PFSS extrapolation and the existence of a unique minimum for the associated inverse problem. This work provides a mathematically rigorous argument for shape optimization based on

PFSS extrapolation in coronal magnetic field modeling, and the proof can extend directly to nonspherical source surface geometries.

3 Observations

In this section, we describe the observations used to formulate the objective functional \mathcal{J} and evaluate the optimization results for estimating R_{ss} . For a given R_{ss} , we calculate the PFSS extrapolation using a synoptic photospheric magnetogram as the inner boundary condition and the source surface at $r = R_{ss}$ as the outer boundary. We then use the radial solar wind velocity from PSP in situ measurements to trace measurements back to source surface footpoints along Parker spiral trajectories. PFSS extrapolation predicts the radial magnetic field at these footpoints, which are then scaled to the spacecraft position and compared with the observed radial magnetic field. This comparison defines the objective functional for estimating R_{ss} . We also use ACE in situ measurements near 1 AU only as an independent dataset to validate R_{ss} and solar cycle trend inferred from the optimization results based on PSP in situ measurements. We therefore describe below the magnetogram, PSP, and ACE observations used in this study.

3.1 Synoptic Magnetograms

In this study, we use the zero point corrected Carrington rotation synoptic magnetograms from the Global Oscillation Network Group (GONG). These magnetograms provide a homogeneous magnetic field boundary input for all PSP encounters considered here, have a grid resolution of 360×180 (Harvey et al., 1996), and are updated daily, making them suitable for the repeated PFSS extrapolations required by the present inverse problem.

There are other products, such as synoptic magnetograms from the Helioseismic and Magnetic Imager (HMI) onboard the Solar Dynamics Observatory (SDO) (Pesnell et al., 2012; Scherrer et al., 2012), where it could also be used for PFSS extrapolation. For each candidate value of R_{ss} in the optimization, PFSS extrapolation needs to be compared with in situ measurements. Using HMI would either require retaining a higher effective spatial resolution, which increases the computational cost of repeated extrapolations, or applying additional rebinning or smoothing, which introduces another methodological choice beyond the scope of the present study as we specifically restrict our investigation to examination of in situ measurements and R_{ss} . A comparison between optimizations driven by GONG and HMI magnetograms is therefore left for future work.

Table S1 in the Supporting Information illustrates the GONG synoptic magnetograms used for Carrington Rotations 2210-2282, covering PSP Encounters 1-19 and spanning the transition from solar minimum to the ascending phase of solar cycle 25. During this period, PSP approached progressively closer to the Sun, with its perihelion distance decreasing to $11.4R_s$ by Encounter 19, thereby providing increasingly near Sun in situ constraints for the optimization of R_{ss} .

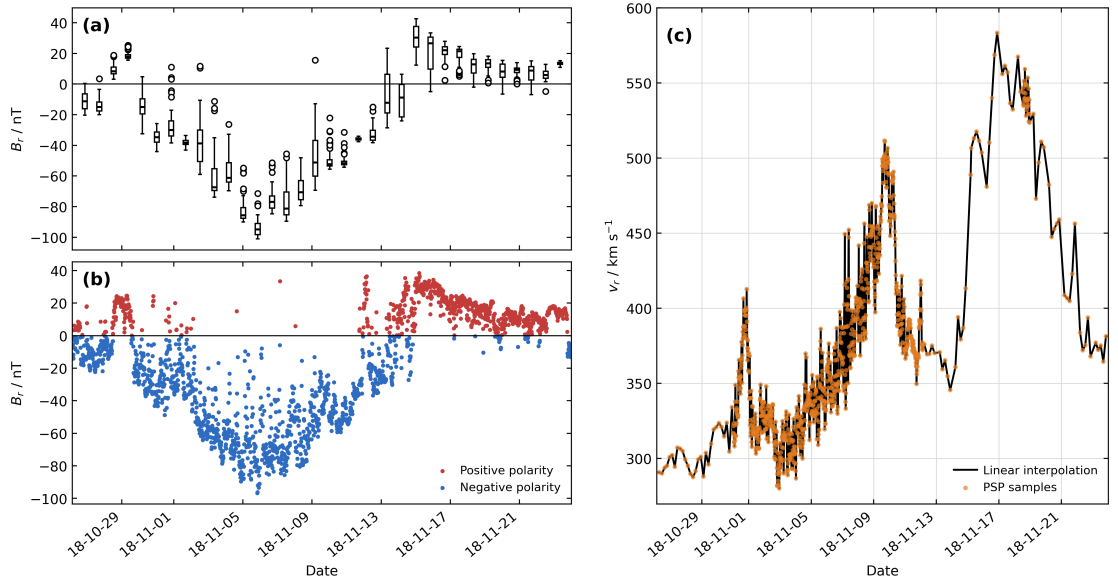


Figure 3: (a) PSP/FIELDS radial magnetic field B_r measurements in hourly time bins for CR2210, shown as boxplots used in the IQR outlier detection, with outliers marked by open circles. (b) PSP/FIELDS B_r after the IQR cleaning and 20 minutes averaging, with red and blue denoting positive and negative polarity, respectively. (c) PSP/SWEAP radial solar wind velocity v_r used for Parker spiral backmapping. The orange points show the PSP samples, and the black curve shows the first order linear interpolation used to fill missing intervals. The time axis spans the full interval of CR2210, whose perihelion occurred on 2018-11-05.

3.2 PSP in situ Measurements

For each PSP encounter, the radial magnetic field and radial solar wind velocity are extracted from PSP in situ measurements during the Carrington rotation that contains the perihelion. This rotation-based selection provides a consistent temporal window for all encounters, emphasizes the near perihelion measurements most relevant to the optimization, and avoids extending the comparison into intervals with data gaps away from perihelion. The FIELDS (Bale et al., 2016) and SWEAP (Kasper et al., 2016; Livi et al., 2022) instruments provide the radial magnetic field and solar wind velocity measurements, respectively, as shown in Figure 3. These measurements are used to constrain the ballistic backmapping and the optimization of R_{ss} . Prior to the optimization, both measurements are averaged to a common temporal cadence. Outliers are removed from the magnetic field measurements, and data gaps in the solar wind velocity series are filled by linear interpolation to provide the continuous velocity input required for backmapping.

For the FIELDS magnetic field measurements, we divide the time series of each encounter into nonoverlapping 1-hour windows and apply the interquartile range (IQR) criterion to identify outliers (Tukey, 1977). Within each window, the first and third quartiles, denoted by Q_1 and Q_3 , are computed, and the interquartile range is defined

as $\text{IQR} = Q_3 - Q_1$. Measurements falling below $Q_1 - 1.5\text{IQR}$ or above $Q_3 + 1.5\text{IQR}$ are flagged as outliers and excluded from the subsequent analysis. Figure 3(a) illustrates this boxplot-based outlier identification for 1-hour windows in CR2210, corresponding to PSP Encounter 1. After outlier removal, the remaining magnetic field measurements are averaged to a 20-minute cadence to reduce short timescale noise. Figure 3(b) shows the resulting magnetic field time series after outlier removal and temporal averaging.

Although PSP provides dense coverage during each encounter, the radial solar wind velocity measured by SPAN-i contains intermittent data gaps. We first resample the velocity measurements to a 1-minute cadence and retain unavailable samples as NaN values. The resulting series is averaged into 20-minute bins, so that short gaps are effectively bridged when neighbouring valid measurements fall within the same bin, while longer intervals with no valid samples remain missing. These remaining gaps are filled by first order linear interpolation, producing a continuous velocity input required for Parker spiral backmapping. Figure 3(c) shows the measured and interpolated radial velocity profiles for CR2210, corresponding to PSP Encounter 1.

In principle, missing intervals in the SPAN-i radial velocity series could be reconstructed using physics-based or data-driven solar wind models, including the WSA model (Arge et al., 2003), artificial neural network approaches (Y. Yang et al., 2018; Y. Yang & Shen, 2019), and convolutional neural network approaches (Lin et al., 2024). These methods are designed primarily to estimate large scale or global solar wind velocity distributions. In contrast, the present analysis requires only a continuous radial velocity series along the PSP trajectory, which is used as an input for Parker spiral backmapping from the spacecraft position to the source surface. Appendix B presents the processed radial magnetic field and solar wind velocity data from PSP Encounters 1-19.

3.3 ACE in situ Measurements

We use in situ measurements from the ACE spacecraft (Stone et al., 1998) for independent cross-validation near 1 AU. We obtain the ACE in situ measurements from the OMNI database and download the ACE Level 2 products AC-H2-MFI and AC-H2-SWI, which provide hourly measurements of the magnetic field and bulk velocity from the Magnetometer (MAG) and the Solar Wind Electron Proton Alpha Monitor (SWEPAM), respectively. Using the encounter windows shown in Table S1, we extract 19 ACE intervals, each corresponding to the Carrington rotation that contains a PSP perihelion. We also apply the same processing procedure to the ACE measurements as to the PSP dataset to ensure consistency between the two in situ datasets. Since ACE remains near the L1 point, it provides nearly continuous solar wind sampling over the selected Carrington rotations in a solar co-rotating coordinates. In the present study, ACE data serves as an independent cross-validation dataset for the optimization results inferred from PSP.

4 Optimization Methodology

This section constructs the optimization framework based on PSP in situ measurements that is used to estimate R_{ss} for PFSS extrapolation. We first define the objective functional as the mean squared error (MSE) between PSP in situ radial magnetic field measurements and the corresponding PFSS extrapolation predictions. For PSP in situ measurements, the spacecraft position is ballistically mapped back to footpoint on the

source surface. The PFSS radial field predictions are then sampled at these footpoints and scaled radially to the PSP heliocentric distance, providing the model prediction used in the MSE. We then describe the optimization algorithm to minimize the objective functional, validate the implementation with an analytical test problem, and define the additional metrics used to evaluate the optimization results.

4.1 PFSS Extrapolation

The classical PFSS extrapolation solves Laplace equation, constrained by an input photospheric magnetogram and a zero potential spherical source surface. The spherical R_{ss} serves as the only tunable parameter in this formulation. The PFSS extrapolation is widely employed in space weather modeling due to its computational efficiency, spatial resolution, and physically feasible approximation of the coronal magnetic structure (Badman et al., 2020). It is commonly solved by spherical harmonic expansion or the finite difference method (FDM) (Toth et al., 2011; Caplan et al., 2021). The spherical harmonic expansion offers the advantage of an explicit analytical solution, enabling direct evaluation of the magnetic potential at arbitrary spatial points without interpolation. It also introduces a free parameter of the maximum Legendre polynomial degree L_{\max} . Higher L_{\max} mainly affects the radial magnetic field from the PFSS extrapolation at smaller heliocentric distances (Toth et al., 2011). FDM requires solutions on a grid followed by spatial interpolation.

In this work, the inverse problem requires repeated PFSS extrapolations for different candidate values of R_{ss} in the optimization. Using FDM would therefore require repeated grid generation and interpolation in different footpoints during the optimization. We therefore use the spherical harmonic expansion and fix $L_{\max} = 22$ throughout the optimization. This choice ensures that changes in the PFSS extrapolation reflect only the variation of R_{ss} rather than harmonic expansion parameters L_{\max} . The complete derivation of the PFSS extrapolation is detailed in Appendix A.

4.2 Objective Functional

For each candidate value of R_{ss} , we use radial solar wind velocity from PSP in situ measurements to trace the spacecraft position \mathcal{O} to their footpoints $\mathcal{Q} = \mathcal{S}(\mathcal{O})$ along Parker spiral lines. We construct this mapping \mathcal{S} in Heliographic Carrington (HG) coordinates, and give the corresponding formulae in Appendix B. We denote the radial magnetic field $B_r^{\text{PFSS},k}$ as the PFSS extrapolation at the source surface footpoint for the same encounter index k . Under the assumption used in the PFSS extrapolation that the magnetic field is radial on the source surface, the radial magnetic field predictions at the PSP position are obtained by scaling R_{ss} with heliospheric distance $r_{\mathcal{O}}$ as,

$$r_{\mathcal{O}}^2 B_r^k(\mathcal{O}) = R_{ss}^2 B_r^{\text{PFSS},k}(\mathcal{S}(\mathcal{O})) \quad \text{for } k = 1, 2, \dots, 19, \quad (14)$$

where B_r^k are the corresponding radial magnetic field predictions from the PFSS extrapolations at the spacecraft position. We then calculate the MSE between the PSP in situ measurements $B_r^{\text{PSP},k}$ and B_r^k to construct the objective functional for the optimization algorithm.

To make the objective functional dimensionless for removing encounter dependent differences in mean level and amplitude, we first apply Z-score normalization to both

$B_r^{\text{PSP},k}$ and B_r^k for each encounter k as follows.

$$\tilde{B}_r^{\text{PSP},k} = \frac{B_r^{\text{PSP},k} - \mu^k}{\sigma^k}, \quad \tilde{B}_r^k = \frac{B_r^k - \mu^k}{\sigma^k} \quad \text{for } k = 1, 2, \dots, 19, \quad (15)$$

where $\tilde{B}_r^{\text{PSP},k}$ and \tilde{B}_r^k denote the normalized observed and modeled radial magnetic field, and μ^k and σ^k are the mean and standard deviation of the $B_r^{\text{PSP},k}$. This normalization subtracts the encounter-specific mean and rescales the magnetic field time series by its characteristic amplitude before the MSE is evaluated. The objective functional measures the agreement in the normalized temporal variation rather than being dominated by differences in the absolute magnetic field amplitude among encounters. It also brings the objective values and their gradients to similar numerical ranges for different encounters, which improves the conditioning of the optimization problem and allows fixed numerical settings, such as the step size and stopping tolerance, to be applied more consistently across encounters.

For encounter k , the continuous objective functional is defined as

$$\tilde{\mathcal{J}}^k = \frac{1}{2} \int_{I_k} |\tilde{B}_r^k(\mathcal{O}_t) - \tilde{B}_r^{\text{PSP},k}(\mathcal{O}_t)|^2 dt \quad \text{for } k = 1, 2, \dots, 19, \quad (16)$$

where I_k denotes the observation interval for the k th PSP encounter. For the discrete time series used in the optimization, the objective functional is defined as

$$\mathcal{J}^k = \frac{1}{2N_k} \sum_{i=1}^{N_k} |\tilde{B}_r^k(\mathcal{O}_{t_i}) - \tilde{B}_r^{\text{PSP},k}(\mathcal{O}_{t_i})|^2 \quad \text{for } k = 1, 2, \dots, 19, \quad (17)$$

where N_k is the number of valid time samples in the k th encounter.

4.3 Optimization Strategy

4.3.1 Optimization Algorithm

The continuity of \mathcal{J}^k with respect to C^2 perturbations of the boundary provides the foundation for treating the determination of R_{ss} as a PDE-constrained inverse problem. Several numerical strategies could in principle be used for this class of problems, including classical gradient-based iterative methods (Nurbekyan et al., 2022) and physics informed neural network that jointly optimize the PDE solution and unknown parameters (Raissi et al., 2019; Cuomo et al., 2022; Song et al., 2024). In the present study, the inverse problem involves only a single scalar parameter R_{ss} . We therefore adopt a direct gradient-based iterative scheme, which is sufficient for the low dimensional optimization considered here and avoids the additional complexity of a neural network for PDE solver. We solve the inverse problem about R_{ss} with the iterative procedure summarized in Algorithm 1. The algorithm minimizes the discrete objective functional \mathcal{J}^k in Eq.17 and returns the corresponding preferred R_{ss} .

For a given R_{ss}^p , the algorithm first calculates $B_r^{\text{PFSS},k}$ once, traces PSP position \mathcal{O}_t to corresponding source surface footpoints \mathcal{Q}_t , samples the PFSS extrapolation $B_r^{\text{PFSS},k}$ at \mathcal{Q}_t , radially scales $B_r^{\text{PFSS},k}(\mathcal{Q}_t)$ to $B_r^k(\mathcal{O}_t)$ at the spacecraft position, dimensionlessly normalizes B_r^k and $B_r^{\text{PSP},k}$, and updates \mathcal{J}^k . We then approximate the gradient with respect to R_{ss} by a centered finite difference with increment Δh and update the radius by

$$R_{ss}^{p+1} = R_{ss}^p - \eta \nabla \mathcal{J}(R_{ss}^p).$$

Algorithm 1 Gradient Based Optimization of R_{ss} with PSP in situ Measurements

Require: $B_r^{\text{PSP},k}$ (radial magnetic field from PSP's FIELDS)
1: $v_r^{\text{PSP},k}$ (radial velocity from PSP's SWEAP)
2: B_γ^k (Carrington heliospheric magnetograms from GONG)
3: R_{ss}^0 (initial R_{ss})
4: N_k (number of valid time samples in encounter k)
5: μ^k (mean value of $B_r^{\text{PSP},k}$ for each encounter)
6: σ^k (standard deviations of $B_r^{\text{PSP},k}$ for each encounter)
7: Δh (finite difference increment used to approximate $\nabla \mathcal{J}$ by centered differences)
8: η (gradient descent step size)
9: N_{max} (maximum number of iterations)
10: ϵ (convergence criterion)
Ensure: R_{ss}^{opt} (optimized R_{ss})
11: $p \leftarrow 0$ ▷ set the iteration index to zero
12: $R_{ss}^p \leftarrow R_{ss}^0 = 1.700R_s$ ▷ set the initial R_{ss}
13: **repeat**
14: $\mathcal{J} \leftarrow 0$ ▷ initialize the objective functional \mathcal{J}
15: $\nabla \mathcal{J} \leftarrow 0$ ▷ initialize the gradient $\nabla \mathcal{J}$
16: $B_r^{\text{PFSS},k} \leftarrow \text{PFSS}(B_\gamma^k, R_{ss}^p)$ ▷ compute the PFSS extrapolation for the current trial radius
17: **for** $t = 1$ **to** N_k **do** ▷ loop over the valid samples in encounter k
18: $\mathcal{O}_t \leftarrow \text{PSP orbit}$ ▷ read the PSP position in HG coordinates
19: $\mathcal{Q}_t \leftarrow \mathcal{S}(\mathcal{O}_t)$ from $v_r^{\text{PSP},k}(t)$ and R_{ss}^p ▷ Parker spiral tracing to the source surface
20: $B_r^{\text{PFSS},k}(\mathcal{Q}_t) \leftarrow B_r^{\text{PFSS},k}, \mathcal{Q}_t$ ▷ take $B_r^{\text{PFSS},k}$ at the traced \mathcal{Q}_t
21: $B_r^k(\mathcal{O}_t) = B_r^{\text{PFSS},k}(\mathcal{Q}_t) \cdot \left(\frac{R_{ss}^p}{r_{\mathcal{O}_t}}\right)^2$ ▷ propagate the radial field to the spacecraft distance
22: $\tilde{B}_r^{\text{PSP},k} = \frac{B_r^{\text{PSP},k} - \mu^k}{\sigma^k}, \tilde{B}_r^k = \frac{B_r^k - \mu^k}{\sigma^k}$ ▷ apply Z score normalization
23: $\delta_t \leftarrow \tilde{B}_r^{\text{PSP},k}(\mathcal{O}_t) - \tilde{B}_r^k(\mathcal{O}_t)$ ▷ evaluate the residual at sample t
24: $\mathcal{J} \leftarrow \mathcal{J} + \delta_t^2$ ▷ accumulate the squared data misfit
25: **end for**
26: $\mathcal{J} \leftarrow \frac{\mathcal{J}}{2N_k}$ ▷ evaluate the discrete objective functional
27: $R_{ss}^+ \leftarrow R_{ss}^p + \Delta h$ ▷ Δh is the finite difference increment
28: $R_{ss}^- \leftarrow R_{ss}^p - \Delta h$
29: $\nabla \mathcal{J} \leftarrow \frac{\mathcal{J}(R_{ss}^+) - \mathcal{J}(R_{ss}^-)}{2\Delta h}$ ▷ centered finite difference approximation
30: $R_{ss}^{p+1} \leftarrow R_{ss}^p - \eta \nabla \mathcal{J}$ ▷ update R_{ss}
31: $p \leftarrow p + 1$
32: **until** $|\nabla \mathcal{J}| < \epsilon$ **or** $p \geq N_{\text{max}}$
33: **return** R_{ss}^p ▷ return the optimized R_{ss}

The iteration stops when $|\nabla \mathcal{J}| < \epsilon$, which indicates that the update has approached a stationary point of the objective functional, or when the iteration count reaches the prescribed upper bound N_{\max} .

To test the optimization algorithm, we construct a synthetic PFSS problem using an analytic potential field. A reference R_{ss} is prescribed, and radial magnetic field samples are generated from the analytic solution along the PSP Encounter 1 trajectory. The optimization is then applied to these synthetic data to determine whether the algorithm can recover the prescribed reference value of R_{ss} . The algorithmic parameters, including the step size η , tolerance ϵ , and maximum iteration number N_{\max} , are adjusted in this test to assess convergence and robustness.

4.3.2 Validation

Here we demonstrate and validate Algorithm 1 both with an analytical test problem, and as applied to PSP Encounter 1 as an example. The results of these optimizations are shown in Figure 4. We first validate the numerical implementation with a test based on an analytic potential for the PFSS extrapolation (Caplan et al., 2021; X. Liu et al., 2022),

$$\psi_1(r, \theta, \phi) = r \left[\left(\frac{1}{R_{ss}} \right)^3 - \left(\frac{1}{r} \right)^3 \right] (\cos \theta + \sin \theta \cos \phi), \quad (18)$$

where $r \in [1, R_{ss}]$, $\theta \in [0, \pi]$, $\phi \in [0, 2\pi)$. We express R_{ss} in units of the solar radius R_s , so that it is treated as a dimensionless optimization variable. The analytic potential ψ_1 satisfies the Laplace equation with mixed boundary conditions, and the corresponding magnetic field is defined by $\mathbf{B} = -\nabla \psi_1$. Its spherical components are given by

$$\begin{cases} B_r(r, \theta, \phi) = \left[(R_{ss})^{-3} + 2r^{-3} \right] (\cos \theta + \sin \theta \cos \phi), \\ B_\theta(r, \theta, \phi) = \left[r^{-3} - (R_{ss})^{-3} \right] (\sin \theta - \cos \theta \cos \phi), \\ B_\phi(r, \theta, \phi) = \left[r^{-3} - (R_{ss})^{-3} \right] \sin \phi. \end{cases} \quad (19)$$

We use this analytic solution to construct a synthetic inverse problem for R_{ss} . A reference value R_{ss}^{ref} is prescribed, and synthetic radial magnetic field samples are generated from ψ_1 along the PSP Encounter 1 trajectory. To mimic observational uncertainty, we add 20% Gaussian noise to these synthetic samples. The same objective functional as in Algorithm 1 is then used to recover the prescribed value R_{ss}^{ref} .

Figure 4(a) shows the convergence process of the optimization, while Figure 4(b) compares the reconstructed radial magnetic field profiles obtained during the iterations with the synthetic reference data. For the case shown in Figure 4(a), we set the initial guess to $R_{ss}^0 = 1.700$, use the step size $\eta = 0.03$, and set the maximum number of iterations to $N_{\max} = 100$. The optimization converges to R_{ss}^{ref} within 20 iterations. This analytic test therefore verifies that the numerical implementation can recover a prescribed R_{ss} from synthetic observations.

We further validate the optimization algorithm using a family of analytic PFSS test fields constructed from individual spherical harmonic modes (Stansby & Verscharen,

Table 1: Analytical Validation Cases for the Optimization Algorithm

l	m	R_{ss}^{ref}	Recovered Value	g_l^m	h_l^m	Iteration Cap
1	0	$2.000R_s$	$2.003R_s$	1.288	0.000	150
1	1	$2.000R_s$	$2.000R_s$	0.148	-0.141	150
2	0	$2.000R_s$	$2.000R_s$	0.192	0.000	150
2	1	$2.000R_s$	$2.001R_s$	-0.089	0.075	150
2	2	$2.000R_s$	$1.998R_s$	-0.320	-0.158	150
5	0	$2.000R_s$	$2.000R_s$	0.968	0.000	150
5	3	$2.000R_s$	$2.000R_s$	0.500	-0.157	150
5	5	$2.000R_s$	$2.000R_s$	0.427	0.544	150
10	0	$2.000R_s$	$1.999R_s$	-0.062	0.000	500
10	5	$2.000R_s$	$2.001R_s$	-0.121	-0.031	500
10	10	$2.000R_s$	$2.000R_s$	-0.463	-0.143	500

This table lists analytical validation cases for selected spherical harmonic modes.

2022). For each degree l and order m , with $l \geq 1$ and $0 \leq m \leq l$, we define

$$\text{Test} = \left\{ \mathbf{B}_l^m \mid \mathbf{B}_l^m = ((B_r)_l^m, (B_\theta)_l^m, (B_\phi)_l^m) \right\}, \quad (20)$$

where the spherical components are given by

$$(B_r)_l^m(r, \theta, \phi) = c_l(r) P_l^m(\cos \theta) (g_l^m \cos m\phi + h_l^m \sin m\phi), \quad (21)$$

$$(B_\theta)_l^m(r, \theta, \phi) = -d_l(r) \frac{\partial P_l^m(\cos \theta)}{\partial \theta} (g_l^m \cos m\phi + h_l^m \sin m\phi), \quad (22)$$

and

$$(B_\phi)_l^m(r, \theta, \phi) = d_l(r) \frac{m P_l^m(\cos \theta)}{\sin \theta} (g_l^m \sin m\phi - h_l^m \cos m\phi). \quad (23)$$

Here P_l^m denotes the associated Legendre function, g_l^m and h_l^m are the mode coefficients, and the radial factors are

$$c_l(r) = \left(\frac{R_s}{r} \right)^{l+2} \frac{(l+1)(R_{ss})^{2l+1} + lr^{2l+1}}{(l+1)(R_{ss})^{2l+1} + l(R_s)^{2l+1}}, \quad (24)$$

$$d_l(r) = \left(\frac{R_s}{r} \right)^{l+2} \frac{(R_{ss})^{2l+1} - r^{2l+1}}{(l+1)(R_{ss})^{2l+1} + l(R_s)^{2l+1}}. \quad (25)$$

Using this analytic test family, we examine individual modes with $l = 1, 2, 5$, and 10, together with selected admissible orders m . For each mode, synthetic radial magnetic field samples are generated with a prescribed reference value $R_{ss}^{\text{ref}} = 2.0R_s$, and the optimization algorithm is then applied to recover R_{ss} from these data. As shown in Table

1, the prescribed value $R_{ss}^{\text{ref}} = 2.0R_s$ is recovered within the expected numerical tolerance for all listed cases. For the higher degree modes, we allow larger maximum iteration numbers, $N_{\text{max}} = 150$ or 500 , to ensure convergence under the chosen validation settings.

These tests verify that the optimization algorithm can recover a prescribed R_{ss} from analytic PFSS data across multiple spherical harmonic modes. They also clarify that, in this validation setting, the inferred change in open field behavior is controlled by the R_{ss} itself, while L_{max} is kept fixed and does not serve as an additional optimization parameter.

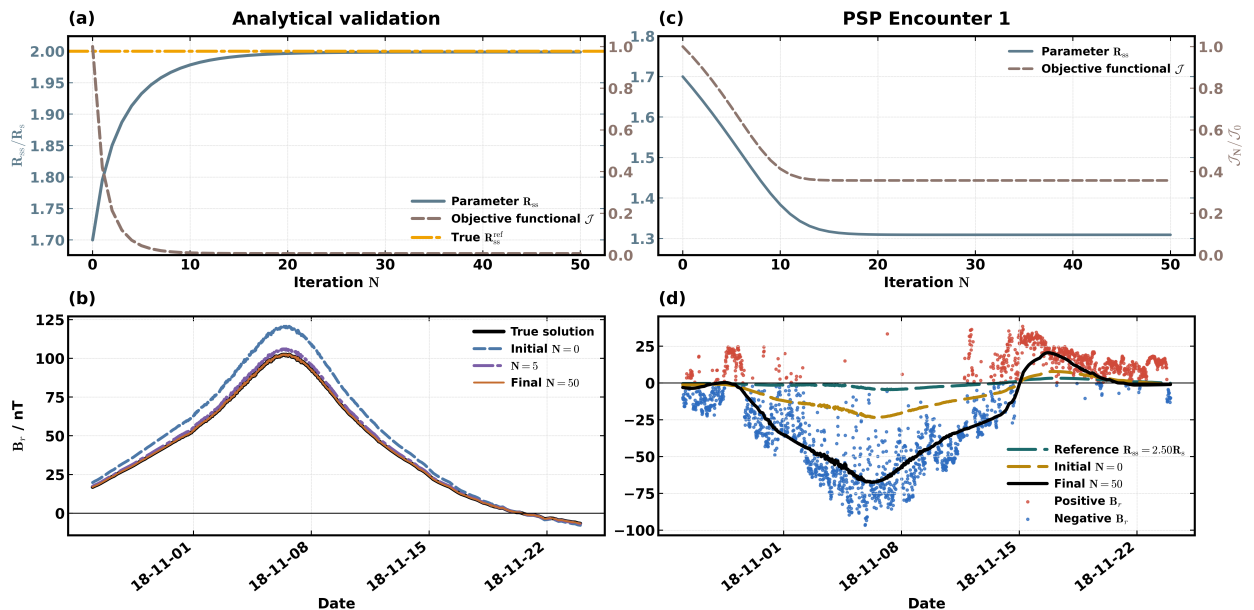


Figure 4: (a) Iteration process for the analytical validation. The blue gray curve shows the evolution of R_{ss} , the brown dashed curve shows the normalized objective functional, and the orange horizontal line marks the prescribed reference value $R_{ss}^{\text{ref}} = 2.0R_s$. (b) Analytical reconstruction of B_r at selected iterations. The black solid curve denotes the true solution, the blue dashed curve denotes the initial state $N = 0$, the purple dash dot curve denotes the intermediate state $N = 5$, and the orange solid curve denotes the final state $N = 50$. (c) Iteration process for PSP Encounter 1. The blue gray curve shows the evolution of R_{ss} , and the brown dashed curve shows the normalized objective functional. (d) Comparison between the $B_r^{\text{PSP},1}$ and B_r^1 for $2.5R_s$ and optimized solutions. Red and blue points denote positive and negative observed $B_r^{\text{PSP},1}$, respectively; the dark gray dashed curve denotes the reference case $R_{ss} = 2.5R_s$, the blue dashed curve denotes the initial state $N = 0$, and the black solid curve denotes the final state $N = 50$.

We next apply the validated optimization algorithm to PSP Encounter 1 and use the numerical settings in Algorithm 1: $R_{ss}^0 = 1.70R_s$, $\eta = 0.5$, $\epsilon = 10^{-5}$, and $N_{\text{max}} = 100$. Figures 4(c) and 4(d) show the optimization result for PSP Encounter 1. Figure 4(c) presents the convergence process of R_{ss} during the iteration. Figure 4(d) compares

$B_r^{\text{PSP},1}$ with two PFSS predictions: the optimized solution and the fixed reference solution obtained with the commonly used value $R_{ss} = 2.5R_s$. The optimization converges to a preferred value of $R_{ss} = 1.31R_s$ for Encounter 1. Compared with the fixed $2.5R_s$ reference case, the optimized solution reduces the mismatch with $B_r^{\text{PSP},1}$. This inferred value is consistent with R_{ss} of approximately $1.3R_s$ reported for PSP Encounter 1 by Badman et al. (2020).

4.4 Additional Evaluation Metrics

We use two additional metrics to interpret the optimal R_{ss} and to identify the dominant factor controlling the optimization results obtained from Algorithm 1. These metrics are the magnetic field scaling factor α^k and the polarity prediction accuracy P_a^k . The magnetic field scaling factor is defined as

$$\alpha^k = \max_{\mathcal{O}} \left| \frac{B_r^{\text{PSP},k}(\mathcal{O})}{B_r^k(\mathcal{O})} \right|, \quad k = 1, 2, \dots, 19, \quad (26)$$

where the maximum is taken over the valid samples in the k th encounter. This metric quantifies the amplitude correction required to bring B_r^k to $B_r^{\text{PSP},k}$ amplitude scale. For PFSS extrapolation, α^k is commonly larger than 1, reflecting the tendency of the model to underestimate the radial magnetic field strength. This tendency is closely related to the open flux problem, in which coronal magnetic field models underestimate the amount of open magnetic flux in the heliosphere (Linker et al., 2017). Reducing R_{ss} generally increases the modeled open flux, thereby increasing B_r^k amplitude. The scaling factor α^k therefore serves as an evaluation metric for interpreting the optimal R_{ss} , if the optimization tends to favor R_{ss} that reduce the amplitude mismatch between B_r^k and $B_r^{\text{PSP},k}$.

The polarity prediction accuracy P_a^k is then used as another evaluation metric to assess whether the optimized solution also improves the agreement in magnetic polarity. While α^k measures the amplitude discrepancy as a regression-driven metric between the PFSS prediction and the PSP measurements, P_a^k depends only on the sign of B_r as a classification-driven metric. It therefore evaluates whether the model reproduces the magnetic sector structure and polarity reversals encountered along the spacecraft trajectory. We define

$$P_a^k = \frac{1}{N_k} \sum_{i=1}^{N_k} \delta(\text{sign}(B_r^k(\mathcal{O}_{t_i})), \text{sign}(B_r^{\text{PSP},k}(\mathcal{O}_{t_i}))), \quad k = 1, 2, \dots, 19, \quad (27)$$

where N_k is the number of valid samples in the k th encounter, and $\delta(a, b) = 1$ if $a = b$ and $\delta(a, b) = 0$ otherwise. Both α^k and P_a^k are computed after the optimization. They are then used in the multiobjective analysis to determine whether the optimal R_{ss} are primarily driven by amplitude agreement or by polarity agreement.

4.5 Pareto Optimal Algorithm

The single objective functional in Eq. 17 defines the optimization problem solved in Algorithm 1. This choice is appropriate for inferring R_{ss} from PSP in situ measurements, but it does not exhaust the possible evaluations of PFSS extrapolations performance. In previous studies, PFSS extrapolations have been evaluated or constrained using several observational quantities, including the IMF strength, open magnetic flux, IMF polarity,

coronal hole areas observed in AIA 193 Å images, and magnetic topology inferred from TSE white light observations (Lee et al., 2011; Arden et al., 2014; Badman et al., 2020; Habbal et al., 2021; Badman et al., 2022; Benavitz et al., 2024). Because these quantities measure different aspects of the heliospheric and coronal magnetic field, they may prefer different R_{ss} . A value of R_{ss} that improves the amplitude agreement may not simultaneously maximize the polarity prediction accuracy. Accordingly, after the single objective optimization has been completed, we perform a multiobjective analysis to quantify the tradeoff between the evaluation metrics and to assess whether the optimized solutions are mainly driven by amplitude or polarity.

A candidate solution is Pareto optimal if one objective cannot be improved without worsening at least one other objective. The set of all such nondominated solutions is called the Pareto optimal set, and its image in the objective space is the Pareto frontier (Miettinen, 1999; Deb, 2001). In the present study, we use Pareto analysis as a posterior evaluation to examine the tradeoff between the amplitude and the polarity agreement. This analysis helps determine whether the optimal R_{ss} obtained from Algorithm 1 are primarily associated with improved consistency.

For each PSP encounter, we consider the parameter interval $\mathcal{X} = [1.2R_s, 3.0R_s]$ and define two objectives. The first objective is the single objective functional \mathcal{J}^k defined in Eq. 17. The second objective is the polarity prediction error, $1 - P_a^k$, where P_a^k is defined in Eq. 27. Thus, the multiobjective problem is written as

$$\min_{R_{ss} \in \mathcal{X}} (\mathcal{J}^k(R_{ss}), 1 - P_a^k(R_{ss})), \quad (28)$$

where both components are minimized.

The scaling factor α^k is not included as an objective in the Pareto construction. Instead, it is retained as a dominant metric for interpreting the resulting Pareto solutions and the optimal R_{ss} . The polarity objective is piecewise constant and does not satisfy the continuity assumptions used in Theorem 2.2. In practice, we sample R_{ss} over \mathcal{X} for PSP Encounters 1-19, evaluate the two objectives at each sampled value, and identify the nondominated points to obtain a discrete approximation of the Pareto optimal set and its frontier. We next define the dominance relation used in this construction.

Definition 6 (Dominance Relation). *For two candidate solutions $R_{ss}^{(1)}, R_{ss}^{(2)} \in \mathcal{X}$, we say that $R_{ss}^{(1)}$ dominates $R_{ss}^{(2)}$, denoted as $R_{ss}^{(1)} \prec R_{ss}^{(2)}$, if and only if*

$$\mathcal{J}^k(R_{ss}^{(1)}) \leq \mathcal{J}^k(R_{ss}^{(2)}), \quad 1 - P_a^k(R_{ss}^{(1)}) \leq 1 - P_a^k(R_{ss}^{(2)}), \quad \text{and} \quad (29)$$

$$\mathcal{J}^k(R_{ss}^{(1)}) < \mathcal{J}^k(R_{ss}^{(2)}) \quad \text{or} \quad 1 - P_a^k(R_{ss}^{(1)}) < 1 - P_a^k(R_{ss}^{(2)}) \quad (30)$$

Definition 7 (Nondominated Set). *A set $\mathcal{ND} \subseteq \mathcal{X}$ is called a non dominated set if*

$$\forall R_{ss}^{(1)}, R_{ss}^{(2)} \in \mathcal{ND}, \quad R_{ss}^{(1)} \not\prec R_{ss}^{(2)} \quad \text{and} \quad R_{ss}^{(2)} \not\prec R_{ss}^{(1)}$$

That is, no solution in \mathcal{ND} dominates any other solution in \mathcal{ND} .

Definition 8 (Pareto Optimal Set). *The Pareto optimal set \mathcal{P}^* is the maximal non dominated subset of \mathcal{X} such that*

$$\mathcal{P}^* = \{R_{ss}^* \in \mathcal{X} \mid \nexists R_{ss} \in \mathcal{X} : R_{ss} \prec R_{ss}^*\}.$$

Equivalently, \mathcal{P}^* consists of all solutions that are not dominated by any other solution in \mathcal{X} .

Definition 9 (Pareto Frontier). *The Pareto frontier \mathcal{F}^* is the image of the Pareto optimal set in the objective space*

$$\mathcal{F}^* = \{(\mathcal{J}^k(R_{ss}^*), 1 - P_a^k(R_{ss}^*)) \in \mathbb{R}^2 \mid R_{ss}^* \in \mathcal{P}^*\}.$$

Several algorithms can construct the Pareto optimal set, including the layering method, the banker’s method, the divide and conquer method, and the quicksort method. We use a quicksort based construction because, after we evaluate the objectives on a discretized parameter set, we can extract the nondominated solutions efficiently from the sorted list.

Algorithm 2 Quicksort Method for Multiobjective Optimization

Require: Parameter space $\mathcal{X} = [R_{\min}, R_{\max}]$, number of evaluations N

Ensure: Pareto optimal set \mathcal{P}^* , Pareto frontier \mathcal{F}^*

Discretize parameter space so that $R_{ss}^{(i)} = R_{\min} + \frac{i-1}{N-1}(R_{\max} - R_{\min})$, $i = 1, \dots, N$

2: **for** $i = 1$ **to** N **do**
 Calculate $\mathcal{J}^{k,(i)} = \mathcal{J}^k(R_{ss}^{(i)})$ using Equation (17)

4: Calculate $E_P^{k,(i)} = 1 - P_a^k(R_{ss}^{(i)})$ using Equation (27)

end for

6: Sort indices by \mathcal{J}^k , namely $\mathbf{I} = \text{argsort}(\{\mathcal{J}^{k,(1)}, \dots, \mathcal{J}^{k,(N)}\})$
 Initialize $\mathcal{P}^* = \emptyset$ and $\min E_P^k = \infty$

8: **for** $t = 1$ **to** N **do**
 $i = I_t$

10: **if** $E_P^{k,(i)} < \min E_P^k$ **then**
 $\mathcal{P}^* \leftarrow \mathcal{P}^* \cup \{R_{ss}^{(i)}\}$

12: $\min E_P^k = E_P^{k,(i)}$

end if

14: **end for**
 Construct $\mathcal{F}^* = \{(\mathcal{J}^{k,(i)}, E_P^{k,(i)}) : R_{ss}^{(i)} \in \mathcal{P}^*\}$ **return** $\mathcal{P}^*, \mathcal{F}^*$

4.6 Reference Simulations

Before applying the optimization, we first perform reference PFSS extrapolations using two fixed R_{ss} at $2.0R_s$ and $2.5R_s$ for PSP Encounters 1-19. These reference cases are evaluated using the same objective functional and evaluation metrics as those used for the optimized solutions. The corresponding results for the PSP and ACE datasets are summarized in Supporting Information Tables S2 and S3, respectively. Here the PSP comparisons provide the direct baseline for the optimization, whereas the ACE comparisons serve as an independent 1 AU validation of the inferred R_{ss} . Together, these fixed R_{ss} simulations provide reference cases against which the improvement achieved by the optimization can be assessed.

5 Results

This section summarizes the optimization results for PSP Encounters 1-19. We begin by presenting the R_{ss} values inferred from Algorithm 1 and relating their evolution to the transition from solar minimum to the ascending phase of solar cycle 25. We then examine deviations from this overall solar activity trend and evaluate the optimized solutions using additional metrics and Pareto analysis. As an independent validation, ACE observations from the corresponding Carrington rotations are used to assess that the results derived from PSP remain consistent with 1 AU measurements.

5.1 Single Objective Optimization

We apply Algorithm 1 by minimizing the objective functional \mathcal{J} in Eq.17. Each run is initialized at $1.70R_s$ and terminated when the convergence criterion is met or when N_{\max} is reached. Figure 5 compares the optimized solutions for PSP Encounters 1-19 with the fixed reference case $R_{ss} = 2.5R_s$.

The optimized solutions generally show better agreement with $B_r^{\text{PSP},k}$ than the fixed R_{ss} reference case. The inferred R_{ss} values also exhibit an overall increase from solar minimum toward the ascending phase of solar cycle 25. This trend can be understood from the amplitude agreement shown in Figure 5. For the earlier encounters, especially those before Encounter 9, the fixed R_{ss} reference solution lies well below the upper envelope of $B_r^{\text{PSP},k}$. This indicates a stronger underestimation of the amplitude by the reference PFSS extrapolation during solar minimum and the early ascending phase. To reduce this amplitude discrepancy, the optimization favors a lower R_{ss} , which increases the amount of open magnetic flux and strengthens B_r^k along the PSP trajectory. For later encounters, the reference solution is closer to the observed upper envelope, so a less required reduction of R_{ss} is required. The resulting optimized R_{ss} therefore increases toward the ascending phase.

This behavior is illustrated in Figure 6. Figure 6(a) compares the reference and optimized PFSS predictions with $B_r^{\text{PSP},k}$ for Encounter 1, representative of solar minimum conditions, and Figure 6(b) shows the corresponding comparison for Encounter 17 during the ascending phase. Because the reference PFSS field is substantially weaker than the observed field during Encounter 1, the optimization favors a lower R_{ss} than in Encounter 17, where the reference solution is already closer to the upper envelope of $B_r^{\text{PSP},k}$.

Not all early encounters follow this amplitude agreement behavior. Within the $k < 9$ group, Encounters 4, 6, and 8 show only limited visible improvement in field amplitude relative to the fixed R_{ss} reference solution. For these cases, the optimal R_{ss} appears to be less strongly controlled by the amplitude agreement and more strongly influenced by the polarity agreement as shown in Table S2. This indicates that the dominant factor selecting the optimal R_{ss} can vary between encounters, with amplitude agreement dominating most early encounters and polarity agreement becoming more important for Encounters 4, 6, and 8.

Figure 7(a) shows the optimal R_{ss} obtained from PSP Encounters 1-19. The red polyline represents the optimization results across the encounters, and the black spline (Dierckx, 1975) is shown as a guide to the overall trend. The blue curve gives the contemporaneous sunspot number as a proxy for solar activity. The R_{ss} generally increase with solar activity, with lower R_{ss} during solar minimum and larger values during the

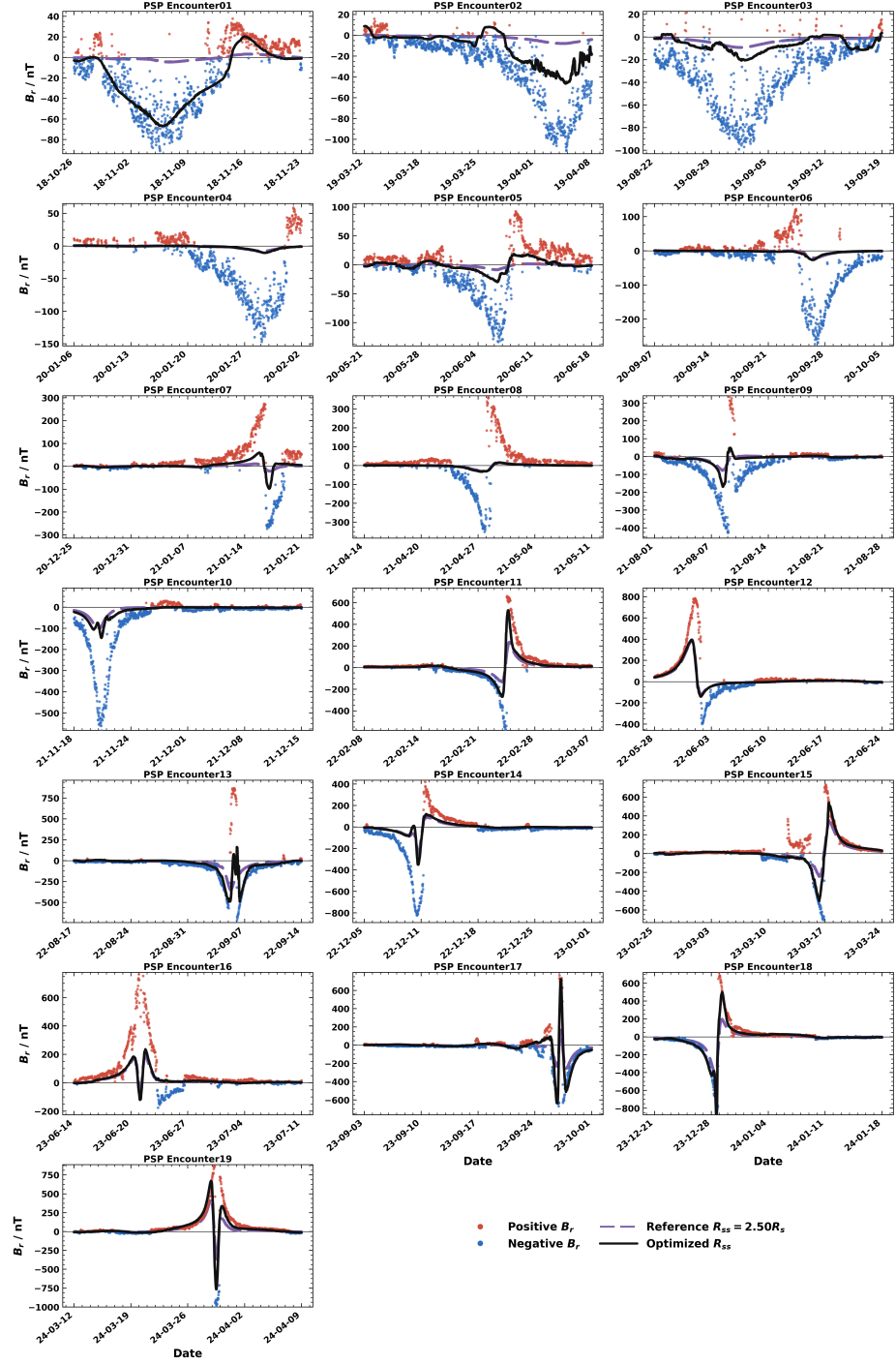


Figure 5: Comparison between $B_r^{\text{PSP},k}$ and B_r^k for Encounters 1-19. Purple curves show the reference solution with $R_{ss} = 2.50R_s$, black curves show the optimized solution from Algorithm 1, and red and blue points denote positive and negative $B_r^{\text{PSP},k}$, respectively.

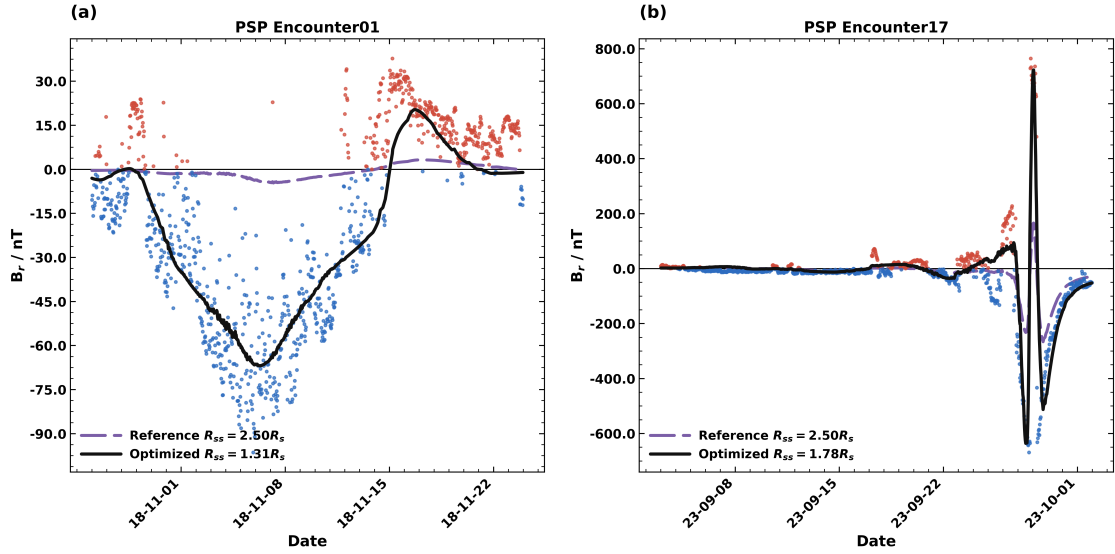


Figure 6: (a) Comparison between $B_r^{\text{PSP},k}$ and B_r^k for PSP Encounter 1 during solar minimum. Red and blue points denote positive and negative $B_r^{\text{PSP},k}$, respectively. The purple dashed curve denotes the reference B_r^k with $R_{ss} = 2.50R_s$, and the black solid curve denotes the optimized solution. (b) Comparison for PSP Encounter 17 during the ascending phase.

ascending phase of solar cycle 25. Figure 7(b) presents the corresponding results obtained from the ACE datasets. The R_{ss} from the ACE datasets exhibit a similar temporal evolution, providing an independent 1 AU validation of the trend inferred from PSP.

5.2 Local Departures from the Overall Trend

Although the overall trend shows a positive correlation between the optimal R_{ss} and solar activity, this trend is not monotonic for every Carrington rotation. Figure 8 highlights two ascending phase examples, Encounters 9 and 13, for which the optimization selects lower R_{ss} values than the surrounding encounters.

Figure 8(a) shows that the optimization for Encounter 9 decreases R_{ss} gradually while the objective functional drops rapidly at early iterations and then approaches a plateau. Figure 8(c) shows that the optimized solution with $R_{ss} = 1.49R_s$ captures more polarity inversions than the reference solution. The analysis of Encounter 9 (see Figure 9) suggests that the local departures from the overall trend are driven by the polarity prediction accuracy. This is because $B_r^{\text{PSP},k}$ for this encounter contains more complex polarity inversions than the other encounters which reference $R_{ss} = 2.5R_s$ fails to capture, and the optimization selects lower R_{ss} values to capture these inversions. These conditions favor inserting more polarity inversions which drives a lower R_{ss} .

Figure 8(b) shows a similar decrease of R_{ss} for Encounter 13, but Figure 8(d) indicates a stronger local departure because the time series contains more complex reversals

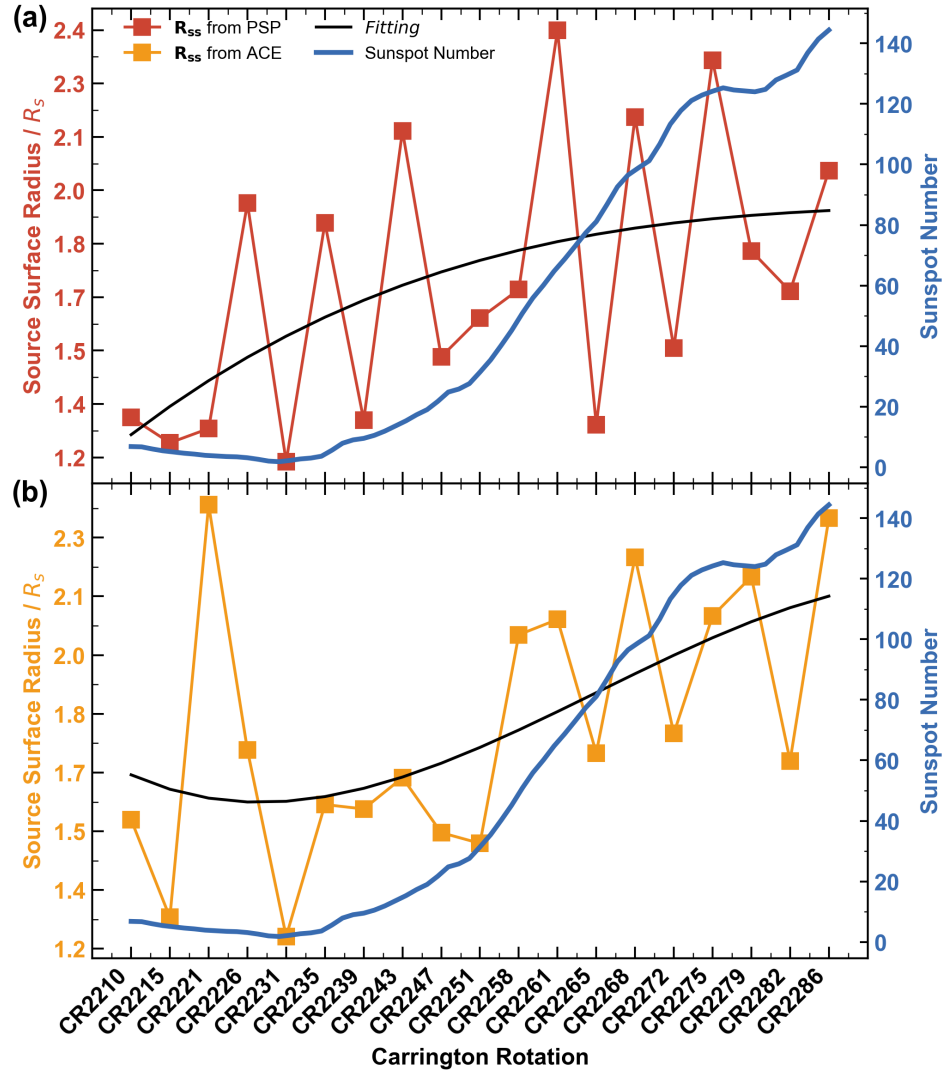


Figure 7: (a) The optimal R_{ss} for PSP Encounters 1-19. The red polyline with square markers shows the encounter by encounter optimization results, the black curve shows the spline used only to visualize the trend, and the blue curve shows the sunspot number over the same Carrington rotation range on the secondary vertical axis. (b) The optimal R_{ss} for ACE datasets. The orange polyline with square markers shows the ACE derived optimal R_{ss} values, the black curve shows the corresponding spline trend, and the blue curve again shows the sunspot number on the secondary vertical axis.

around 5 September 2022 and 6 September 2022. During this interval, PSP crossed an interplanetary coronal mass ejection (ICME) characterized by complex topological structures (Romeo et al., 2023). This event drives the optimal R_{ss} to $1.27R_s$. The application

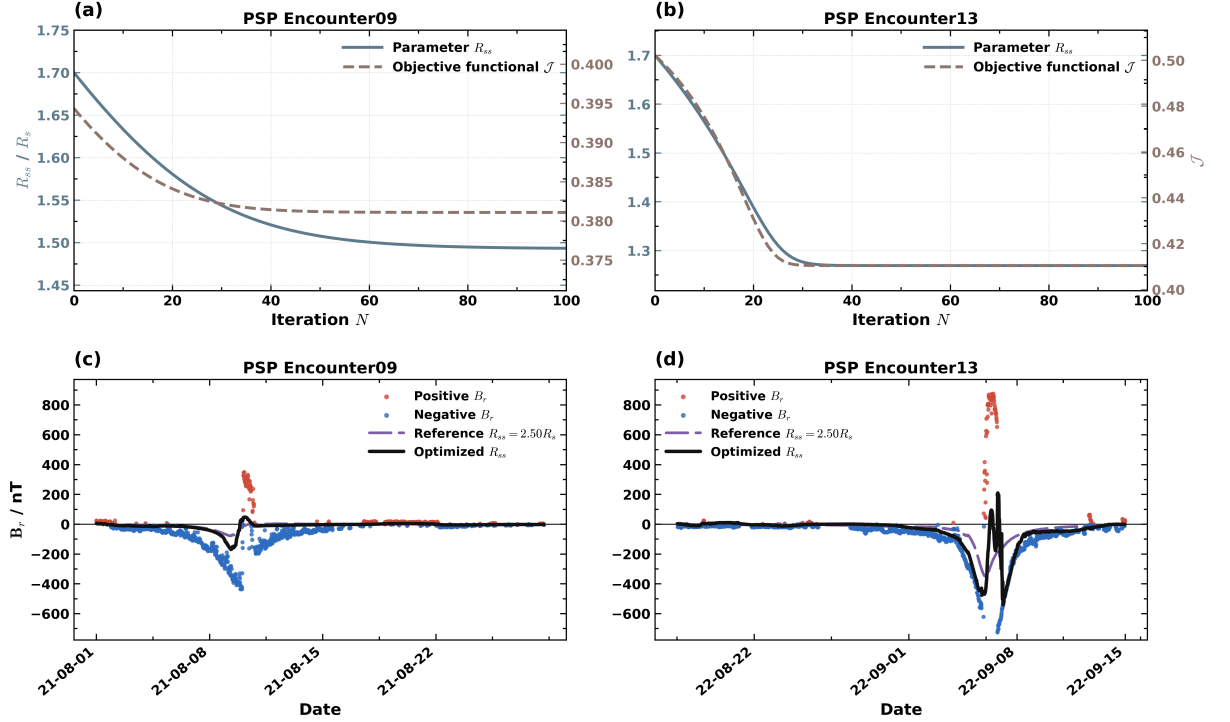


Figure 8: (a) Iteration process for PSP Encounter 9. The blue gray curve shows the evolving parameter R_{ss} , and the brown dashed curve shows the objective functional \mathcal{J} . (b) Iteration process for PSP Encounter 13, with the same curve definitions as in panel (a). (c) Comparison between the $B_r^{\text{PSP},k}$ and B_r^k for Encounter 9. Red and blue points denote positive and negative observed B_r , respectively. The purple dashed curve denotes the reference B_r^k with $R_{ss} = 2.50R_s$, and the black solid curve denotes the optimized B_r^k . (d) Comparison for Encounter 13, with the same curve definitions as in panel (a).

of optimization algorithm to events with CME compromises the meaningful estimation of the optimal R_{ss} . Under these circumstances, spacecraft observations occur within a severely perturbed interplanetary environment where the magnetic field configuration breaks the Parker spiral approximation.

5.3 Open Flux and Polarity Accuracy

We focus here on the two metrics that are not used in the optimization, the open flux Φ_{flux}^k , a meaningful quantity where the ratio of the predicted and measured value is equal to α^k , as defined in section 4.4, and the polarity prediction accuracy P_a^k . In the PFSS extrapolation, the global open flux is obtained by integrating the radial magnetic field over the source surface

$$\Phi_{\text{flux}}^k(R_{ss}) = R_{ss}^2 \int_0^{2\pi} d\phi \int_0^\pi |B_r^{\text{PFSS},k}(R_{ss}, \theta, \phi)| \sin \theta d\theta. \quad (31)$$

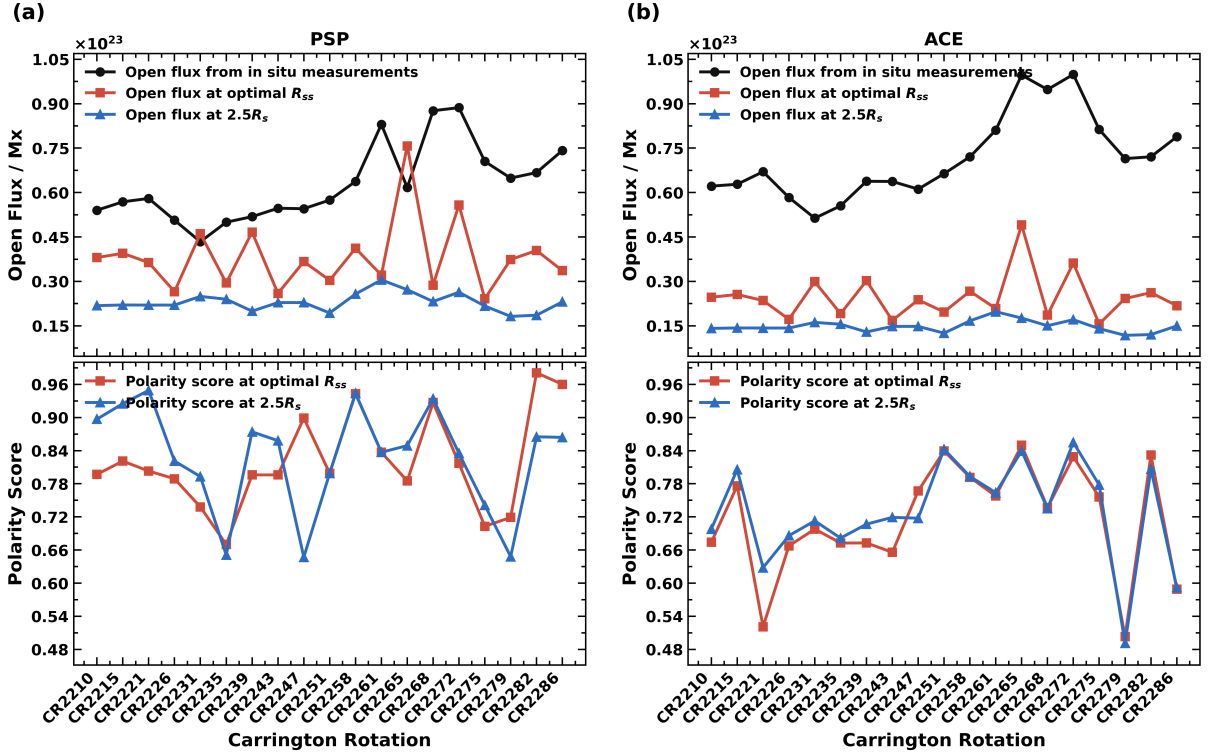


Figure 9: (a) Open flux and polarity prediction accuracy for the PSP based evaluation. The upper plot compares the open flux inferred from PSP in situ measurements, shown by the black curve, with the optimized solution in red and the fixed reference case with $R_{ss} = 2.5R_s$ in blue. The lower plot gives the corresponding polarity prediction accuracy for the optimized and reference solutions. (b) Open flux and polarity prediction accuracy for the ACE based evaluation. The upper plot shows the ACE open flux comparison, where the black curve denotes the in situ estimate and the red and blue curves denote the optimized and reference solutions. The lower plot shows the associated polarity prediction accuracy. Circular markers denote the open flux inferred from in situ measurements, square markers denote the optimized solution, and triangular markers denote the reference solution.

The latitude independent nature of B_r^k (Smith & Balogh, 1995, 2003) suggests that the open magnetic flux estimated from in situ measurements can be formulated as

$$\Phi_H^k = \frac{4\pi}{N} \sum_{i=1}^N \left(r_i^{\text{PSP},k}(\mathcal{O}_i) \right)^2 |B_r^{\text{PSP},k}(\mathcal{O}_i)|. \quad (32)$$

Figure 9(a) shows that the open flux derived from PSP in situ measurements exceeds the open flux from the PFSS extrapolation for both the optimized solution and the fixed reference case $R_{ss} = 2.5R_s$. The optimized solution shows improved agreement with the in situ open flux compared to the reference case, indicating that the optimization

process effectively reduces the open flux discrepancy. The lower plot in Figure 9(a) shows the polarity prediction accuracy P_a^k . For encounters with $k < 9$, P_a^k has a small reduction relative to the reference case, which indicates that the optimization process slightly reduces polarity prediction accuracy for improved open flux agreement. That is, the optimization process for these encounters is more driven by the amplitude agreement than by the polarity agreement. P_a^k is not the dominant metric in selecting the optimal R_{ss} for these encounters. During CR2247, or Encounter 9, the optimized solution improves polarity prediction accuracy which has been the dominant metric for optimization. For encounters with $k \geq 9$, P_a^k remains or improves accuracy. Section 5.4 interprets this behavior as a change in the balance between amplitude agreement and polarity agreement.

Figure 9(b) shows the corresponding ACE evaluation. It follows the same trend as the PSP results and shows higher polarity prediction accuracy during the ascending phase than during solar minimum. That is the lower sensitivity of P_a^k to R_{ss} during the ascending phase. Figure S1 illustrates the global distribution of the source surface magnetic field across varying levels of solar activity. During the ascending phase, the sector structure and the heliospheric current sheet tend to be more inclined relative to the ecliptic, so an ecliptic spacecraft crosses a sector boundary becomes more predictable and less sensitive to modest changes in R_{ss} . During solar minimum, the current sheet is flatter, and small changes in the extrapolated field or mapped trajectory can move the spacecraft from one side of the sector boundary to the other, which makes P_a^k more sensitive to R_{ss} (Badman et al., 2023). Polar field measurements remain poorly constrained from the ecliptic plane, which affects open flux estimates (S. Yang et al., 2024a). This limitation is most important during solar minimum, when long lived polar coronal holes dominate the global magnetic structure (Y.-M. Wang et al., 2009; Hahn et al., 2010; Karna et al., 2014; Pishkalo, 2019; Andreeva, 2023; S. Yang et al., 2024b). Magnetograph calibration (X. Wang et al., 2010) and time dependent contributions from coronal hole boundaries (Arge et al., 2024) may also affect the comparison.

5.4 Pareto Optimal Set for Multiobjective Optimization

We use the Pareto optimal set to evaluate which metric plays the dominant role in selecting the final value of R_{ss} and to clarify why the optimal R_{ss} varies across encounters. The Pareto optimal set consists of the nondominated candidate values of R_{ss} in the parameter space, whereas the Pareto frontier is the image of these candidates in the two-objective space ($\mathcal{J}^k, 1 - P_a^k$). A more dispersed Pareto frontier indicates a stronger conflict between the MSE objective and the polarity prediction error: reducing the MSE requires sacrificing polarity agreement, or improving polarity agreement requires a larger MSE. In this case, the optimization is mainly controlled by the amplitude agreement. By contrast, a more clustered Pareto frontier indicates that the nondominated candidates occupy a narrower region of the objective space. When the MSE values of these candidates become less separated, the polarity prediction error becomes more influential in determining which R_{ss} is preferred.

Figure 10 illustrates this analysis for Encounter 17. Figure 10(a) shows the variation of the objective functional and the polarity prediction error with R_{ss} , together with the corresponding Pareto optimal set in the parameter space. Figure 10(b) maps the same sampled candidate values into the two-objective space and shows the resulting Pareto frontier. Because the MSE objective and the polarity prediction error do not attain a common global minimum, the nondominated candidates form a Pareto opti-

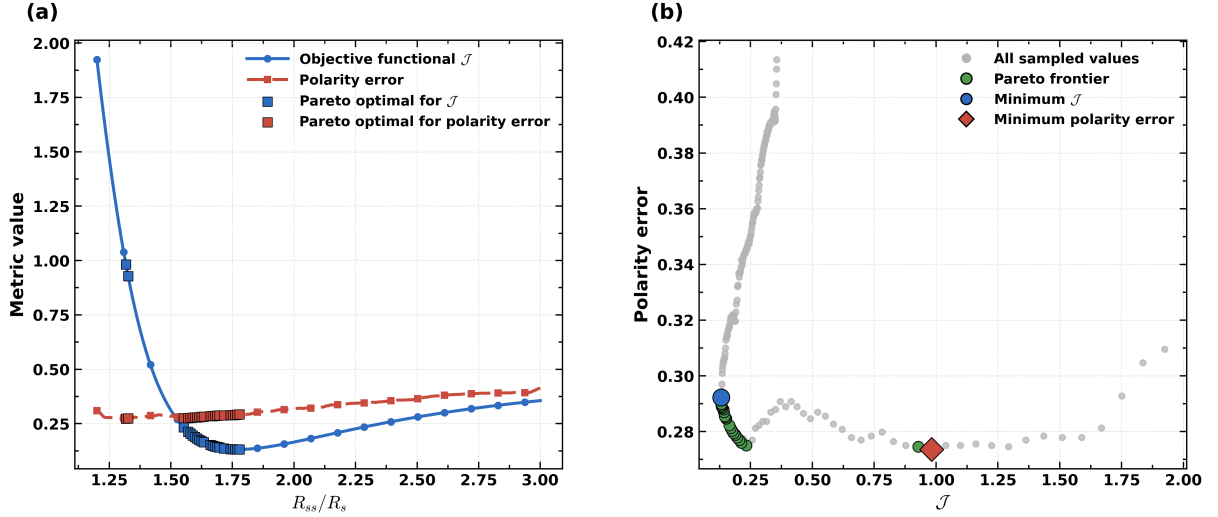


Figure 10: (a) Pareto analysis for PSP Encounter 17 in parameter space. The blue curve shows the objective functional \mathcal{J}^k from Eq.17, and the red dashed curve shows the polarity prediction error $1 - P_a^k$ from Eq.27 as functions of R_{ss} . The blue and red square markers denote the Pareto optimal subsets associated with these two metrics. (b) Pareto frontier for PSP Encounter 17 in the two objective space. The gray points represent all sampled candidate values of R_{ss} , the green circles denote the Pareto frontier, the blue circle marks the global minimum of the objective functional \mathcal{J}^k , and the red diamond marks the global minimum of the polarity prediction error.

mal set rather than a single solution that simultaneously minimizes both objectives. For Encounter 17, the Pareto frontier is relatively clustered, indicating that the admissible tradeoffs are concentrated within a narrow objective range. In this case, the final choice of R_{ss} is more strongly constrained by polarity agreement than by amplitude agreement.

We then apply Algorithm 2 to PSP Encounters 1-19 and show the resulting Pareto frontiers in Figure 11. The gray points denote all sampled values of R_{ss} projected into the objective space $(\mathcal{J}^k, 1 - P_a^k)$, and the green points mark the nondominated candidates that define the discrete Pareto frontier. Each green point represents a candidate R_{ss} for which one objective cannot be improved without degrading the other. The configuration of the frontier therefore reveals the degree of competition between amplitude agreement and polarity agreement.

For the earlier encounters, the Pareto frontiers are more dispersed, indicating a stronger conflict between the two objectives. The polarity metric does not dominate the selection of R_{ss} ; instead, the optimization is mainly driven by amplitude agreement. As solar activity increases, the Pareto frontiers become more clustered in the objective space. This clustering shows that the range of nondominated tradeoffs becomes narrower and that polarity prediction error becomes increasingly important in selecting the preferred R_{ss} . The transition from dispersed to clustered Pareto frontiers therefore indicates

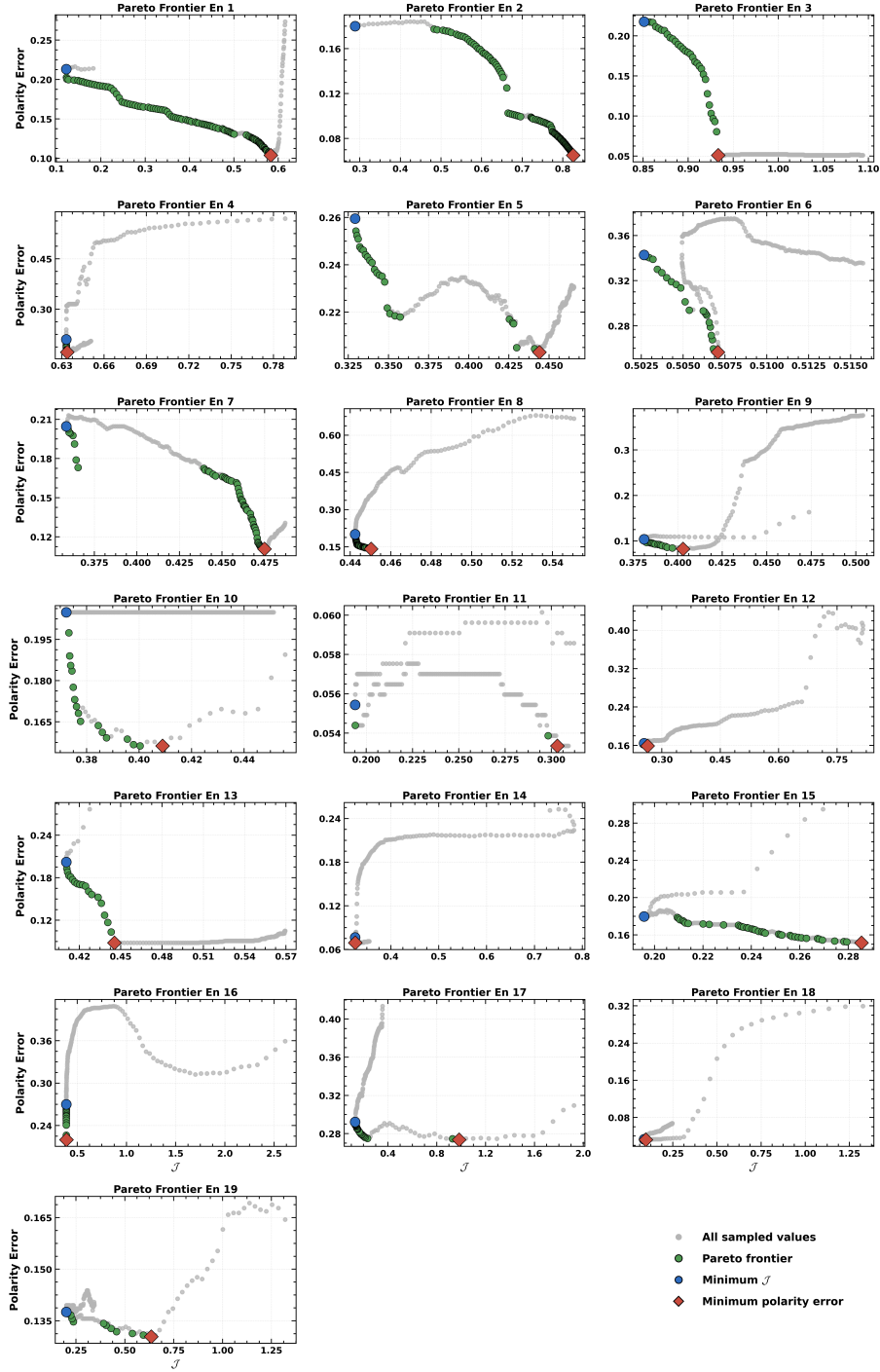


Figure 11: Pareto frontiers for PSP Encounters 1-19 calculated with Algorithm 2. In each panel, the gray points represent all sampled candidate values of R_{ss} in the two objective space, the green circles denote the Pareto frontier, the blue circles mark the minima of the objective functional, and the red diamonds mark the minima of the polarity prediction error. Across the encounter sequence, the frontiers evolve from more dispersed configurations to more clustered ones.

a shift in the dominant metric of the optimization, from amplitude agreement during solar minimum toward polarity agreement during the ascending phase of solar cycle 25.

6 Conclusion

This paper completes the mathematical theory proof and constructs an optimization algorithm for the optimal source surface problem, along with optimization validation and multiobjective optimization analysis.

Section 2 proves the well-posedness of the forward problem for PFSS extrapolation and reformulates the inverse problem for R_{ss} as a free boundary problem. By combining the compactness of the admissible set with continuity of the objective functional, we show that the inverse problem admits at least one minimizer. The arguments can apply to nonspherical source surface geometries as well as to the spherical case used in the present PSP application.

Section 4 also develops and presents Algorithm 1 to perform the optimization. We define the objective functional as a normalized MSE between $B_r^{\text{PSP},k}$ and B_r^k . The algorithm then minimizes this objective functional, and the analytical validation shows that a prescribed reference radius can be recovered from noisy test data. Additional evaluation metrics, including the magnetic field scaling factor and polarity prediction accuracy, are used to interpret the optimized solutions. The Pareto analysis extends this interpretation by quantifying the tradeoff between the objective functional and polarity prediction error.

Overall, the optimal R_{ss} inferred from PSP Encounters 1-19 increase from solar minimum to the ascending phase of solar cycle 25. The same trend is recovered from ACE measurements over the corresponding Carrington rotations. Relative to the fixed reference cases, the optimal R_{ss} reduce the open flux discrepancy and generally preserve or improve the magnetic field polarity agreement. Some encounters depart from the overall trend, especially when polarity reversals or CME disturbed magnetic structure make lower R_{ss} values more favorable under the adopted PFSS extrapolation and Parker spiral assumptions.

Finally, we perform a multiobjective analysis using the MSE objective \mathcal{J} and the polarity prediction error $1 - P_a$. Algorithm 2 is applied to construct the Pareto frontiers for PSP Encounters 1-19. These frontiers are used to evaluate the relative importance of amplitude agreement and polarity agreement in selecting the optimal R_{ss} , and thereby to interpret the mechanisms underlying the variation of R_{ss} across the encounters. This transition from dispersed to clustered Pareto frontiers indicates a shift in the dominant metric from amplitude agreement during solar minimum toward polarity agreement during the ascending phase. It therefore explains why the optimized R_{ss} increases as solar activity strengthens.

By comparisons with TSE white-light topology, relevant studies have represented that optimization according to TSE white light images yield a best R_{ss} which instead decreases during solar maximum. (Altschuler & Newkirk, 1969; Benavitz et al., 2024). Taking these results together shows there is no globally optimal R_{ss} , but instead that optimization is with respect to the predefined metrics. Our optimization enhances both polarity predictions and open flux estimations at various solar activity cycles and indicates that during the solar ascending phases, a higher R_{ss} yields better predictions of

polarity and open flux, whereas improved white-light morphology predictions require the opposite conditions. This discrepancy is summarized by the open flux problem, where (1) physical model cannot simultaneously satisfy multiple independent observations and (2) estimates of open flux from coronal hole observations conflict with those from in-situ measurements (Linker et al., 2021; Asvestari et al., 2024). Besides, we do not incorporate observations from the solar polar regions, which may impose constraints on the estimation of R_{ss} during solar minimum conditions. On the other hand, PFSS extrapolation demonstrates an underestimation of open magnetic flux predictions, which necessitates improvements in coronal model or magnetograms boundary condition (Linker et al., 2017). This underestimation may be improved by incorporating photospheric magnetic field observations from solar polar regions. In fact, continuous in-situ measurements for both northern and southern polar magnetic fields in the inner corona region would improve the performance of our optimization algorithm. Currently, the Solar Orbiter is scheduled to reach an orbital inclination of 33 degrees by July 2029, which will provide support for further redefinition of our optimization framework (Müller et al., 2022). Our future work will focus on two aspects: on the one hand, refining the theoretical framework of shape optimization for coronal magnetic field models; on the other hand, reformulating the coronal magnetic field model to address these limitations.

Conflict of Interest

The authors declare no conflicts of interest relevant to this study.

Open Research

The PFSS extrapolation and optimization algorithm code is available at <https://doi.org/10.5281/zenodo.17129425> (S. Wang, 2025). PSP magnetic field data are available at <https://fields.ssl.berkeley.edu/> and solar wind velocity data are accessible at <http://sweap.cfa.harvard.edu/>. GONG magnetogram data can be obtained from the National Solar Observatory (NSO) at <https://nso.edu/data/nisp-data/>. ACE data are available via the OMNIWeb <https://omniweb.gsfc.nasa.gov/>. All calculations and visualizations in this paper are implemented by using Python 3.9.13, leveraging the numpy (v1.25.2) (Harris et al., 2020), scipy (v1.11.1) libraries (P. Virtanen et al., 2020) for array operations and associated Legendre function computations and astropy.io.fits (v5.3.1) for CDF/FITS format data (Astropy Collaboration et al., 2022), sunpy.map (v5.0.0) for Carrington magnetograms (The SunPy Community et al., 2020) and matplotlib (v3.7.2) for visualizations, available under the Matplotlib license (Hunter, 2007).

Acknowledgments

The work is jointly supported by the NSFC and the National Key R&D Program of China (42330210, 2022YFF0503800, 42004146 and 2021YFA0718600), the Specialized Research Fund for State Key Laboratories, the open project fund of State Key Laboratory of Lunar and Planetary Sciences (Macau University of Science and Technology) (Macau FDCT grant No. 002/2024/SKL), and the Climbing Program of NSSC (E5PD3003). Magnetic field and velocity measurements from the Parker Solar Probe can be accessed through FIELDS and SWEAP, respectively. We obtain the solar wind data measured by the ACE spacecraft from the OMNI database. This work uses GONG data obtained

by the NSO Integrated Synoptic Program, managed by the National Solar Observatory, which is operated by the Association of Universities for Research in Astronomy (AURA), Inc. under a cooperative agreement with the National Science Foundation and with contributions from the National Oceanic and Atmospheric Administration. The GONG network of instruments is hosted by the Big Bear Solar Observatory, High Altitude Observatory, Learmonth Solar Observatory, Udaipur Solar Observatory, Instituto de Astrofísica de Canarias, and Cerro Tololo Interamerican Observatory. The authors gratefully acknowledge these supports.

References

- Acker, A. (1981, June). Interior free boundary problems for the Laplace equation. *Archive for Rational Mechanics and Analysis*, 75(2), 157–168. Retrieved from <https://doi.org/10.1007/BF00250477> doi: 10.1007/BF00250477
- Alt, H., & Schumny, H. (1984). Einführung. In H. Alt & H. Schumny (Eds.), *Maschinenbau (ti-58/59, hp-41 c, fx-502/602 p): Verbindungstechnik, verformungstechnik, getriebetechnik, wärmeabfuhr* (pp. 1–1). Wiesbaden: Vieweg+Teubner Verlag. Retrieved from https://doi.org/10.1007/978-3-322-85906-8_1 doi: 10.1007/978-3-322-85906-8_1
- Altschuler, M. D., & Newkirk, G. (1969, September). Magnetic fields and the structure of the solar corona. *Solar Physics*, 9(1), 131–149. Retrieved from <https://doi.org/10.1007/BF00145734> doi: 10.1007/BF00145734
- Andreeva, O. (2023). Evolutionary features of polar and non-polar coronal holes during solar cycle 24 and the rising phase of cycle 25. *Advances in Space Research*, 71(4), 1915–1921. Retrieved from <https://www.sciencedirect.com/science/article/pii/S0273117722006664> (Recent progress in the physics of the Sun and heliosphere) doi: <https://doi.org/10.1016/j.asr.2022.07.043>
- Arden, W. M., Norton, A. A., & Sun, X. (2014). A “breathing” source surface for cycles 23 and 24. *Journal of Geophysical Research: Space Physics*, 119(3), 1476–1485. Retrieved from <https://agupubs.onlinelibrary.wiley.com/doi/abs/10.1002/2013JA019464> doi: <https://doi.org/10.1002/2013JA019464>
- Arge, C. N., Leisner, A., Antiochos, S. K., Wallace, S., & Henney, C. J. (2024, mar). Proposed resolution to the solar open magnetic flux problem. *The Astrophysical Journal*, 964(2), 115. Retrieved from <https://dx.doi.org/10.3847/1538-4357/ad20e2> doi: 10.3847/1538-4357/ad20e2
- Arge, C. N., Odstrcil, D., Pizzo, V. J., & Mayer, L. R. (2003, September). Improved Method for Specifying Solar Wind Speed Near the Sun. *AIP Conference Proceedings*, 679(1), 190–193. Retrieved from <https://doi.org/10.1063/1.1618574> (_eprint: https://pubs.aip.org/aip/acp/article-pdf/679/1/190/11484695/190_1_online.pdf) doi: 10.1063/1.1618574
- Astropy Collaboration, Price-Whelan, A. M., Lim, P. L., Earl, N., Starkman, N., Bradley, L., ... Astropy Project Contributors (2022, August). The Astropy Project: Sustaining and Growing a Community-oriented Open-source Project and the Latest Major Release (v5.0) of the Core Package. *The Astrophysical Journal*, 935(2), 167. doi: 10.3847/1538-4357/ac7c74
- Asvestari, E., Heinemann, S. G., Temmer, M., Pomoell, J., Kilpua, E., Magdalenic, J., & Poedts, S. (2019). Reconstructing coronal hole areas with euhforia and adapted wsa model: Optimizing the model parameters. *Journal of Geophysical Research: Space Physics*, 124(11), 8280–8297. Retrieved from <https://doi.org/10.1029/2019JA026500>

- agupubs.onlinelibrary.wiley.com/doi/abs/10.1029/2019JA027173 doi:
<https://doi.org/10.1029/2019JA027173>
- Asvestari, E., Temmer, M., Caplan, R. M., Linker, J. A., Heinemann, S. G., Pinto, R. F., ... Samara, E. (2024, aug). Coronal models and detection of the open magnetic field. *The Astrophysical Journal*, 971(1), 45. Retrieved from <https://dx.doi.org/10.3847/1538-4357/ad5155> doi: 10.3847/1538-4357/ad5155
- Badman, S. T., Bale, S. D., Oliveros, J. C. M., Panasenco, O., Velli, M., Stansby, D., ... Whittlesey, P. L. (2020, feb). Magnetic connectivity of the ecliptic plane within 0.5 au: Potential field source surface modeling of the first parker solar probe encounter. *The Astrophysical Journal Supplement Series*, 246(2), 23. Retrieved from <https://dx.doi.org/10.3847/1538-4365/ab4da7> doi: 10.3847/1538-4365/ab4da7
- Badman, S. T., Brooks, D. H., Poirier, N., Warren, H. P., Petrie, G., Rouillard, A. P., ... Wallace, S. (2022, jun). Constraining global coronal models with multiple independent observables. *The Astrophysical Journal*, 932(2), 135. Retrieved from <https://dx.doi.org/10.3847/1538-4357/ac6610> doi: 10.3847/1538-4357/ac6610
- Badman, S. T., Riley, P., Jones, S. I., Kim, T. K., Allen, R. C., Arge, C. N., ... Verniero, J. L. (2023). Prediction and verification of parker solar probe solar wind sources at 13.3 rs. *Journal of Geophysical Research: Space Physics*, 128(4), e2023JA031359. Retrieved from <https://agupubs.onlinelibrary.wiley.com/doi/abs/10.1029/2023JA031359> (e2023JA031359 2023JA031359) doi: <https://doi.org/10.1029/2023JA031359>
- Bale, S. D., Badman, S. T., Bonnell, J. W., Bowen, T. A., Burgess, D., Case, A. W., ... Wygant, J. R. (2019, December). Highly structured slow solar wind emerging from an equatorial coronal hole. *Nature*, 576(7786), 237–242. Retrieved from <https://doi.org/10.1038/s41586-019-1818-7> doi: 10.1038/s41586-019-1818-7
- Bale, S. D., Goetz, K., Harvey, P. R., Turin, P., Bonnell, J. W., Dudok de Wit, T., ... Wygant, J. R. (2016, December). The FIELDS Instrument Suite for Solar Probe Plus. *Space Science Reviews*, 204(1), 49–82. Retrieved from <https://doi.org/10.1007/s11214-016-0244-5> doi: 10.1007/s11214-016-0244-5
- Benavitz, L. F., Boe, B., & Habbal, S. R. (2024, oct). Total solar eclipse white-light images as a benchmark for potential field source surface coronal magnetic field models: An in-depth analysis over a solar cycle. *The Astrophysical Journal*, 974(2), 178. Retrieved from <https://dx.doi.org/10.3847/1538-4357/ad71c6> doi: 10.3847/1538-4357/ad71c6
- Bercic, L., Larson, D., Whittlesey, P., Maksimovic, M., Badman, S. T., Landi, S., ... Stevens, M. L. (2020, apr). Coronal electron temperature inferred from the strahl electrons in the inner heliosphere: Parker solar probe and helios observations. *The Astrophysical Journal*, 892(2), 88. Retrieved from <https://dx.doi.org/10.3847/1538-4357/ab7b7a> doi: 10.3847/1538-4357/ab7b7a
- Bizien, N., Froment, C., Madjarska, M. S., Dudok de Wit, T., & Velli, M. (2025). Tracing magnetic switchbacks to their source: An assessment of solar coronal jets as switchback precursors. *Astronomy Astrophysics*, 694, A181. Retrieved from <https://doi.org/10.1051/0004-6361/202452140> doi: 10.1051/0004-6361/202452140
- Boe, B., Habbal, S., & Druckmüller, M. (2020, jun). Coronal magnetic field topology from total solar eclipse observations. *The Astrophysical Journal*, 895(2), 123. Retrieved from <https://dx.doi.org/10.3847/1538-4357/ab8ae6> doi: 10.3847/1538-4357/ab8ae6

- Caffarelli, L., & Alt, H. (1981). Existence and regularity for a minimum problem with free boundary. *Journal für die reine und angewandte Mathematik*, 1981(325), 105–144. Retrieved 2024-12-03, from <https://doi.org/10.1515/crll.1981.325.105> doi: doi:10.1515/crll.1981.325.105
- Caplan, R. M., Downs, C., Linker, J. A., & Mikic, Z. (2021, jul). Variations in finite-difference potential fields. *The Astrophysical Journal*, 915(1), 44. Retrieved from <https://dx.doi.org/10.3847/1538-4357/abfd2f> doi: 10.3847/1538-4357/abfd2f
- Chang, K.-H. (2015). Chapter 19 - multiobjective optimization and advanced topics. In K.-H. Chang (Ed.), *e-design* (p. 1105-1173). Boston: Academic Press. Retrieved from <https://www.sciencedirect.com/science/article/pii/B9780123820389000193> doi: <https://doi.org/10.1016/B978-0-12-382038-9.00019-3>
- Cuomo, S., Giampaolo, F., Izzo, S., Nitsch, C., Piccialli, F., & Trombetti, C. (2022). A physics-informed learning approach to bernoulli-type free boundary problems. *Computers Mathematics with Applications*, 128, 34-43. Retrieved from <https://www.sciencedirect.com/science/article/pii/S0898122122004266> doi: <https://doi.org/10.1016/j.camwa.2022.10.003>
- Dakeyo, J., Badman, S. T., Rouillard, A. P., Réville, V., Verscharen, D., Démoulin, P., & Maksimovic, M. (2024). Radial evolution of the accuracy of ballistic solar wind backmapping. *Astronomy Astrophysics*, 686, A12. Retrieved from <https://doi.org/10.1051/0004-6361/202348892> doi: 10.1051/0004-6361/202348892
- Dakeyo, J., Rouillard, A. P., Réville, V., Démoulin, P., Maksimovic, M., Chapiron, A., ... Louarn, P. (2024). Testing the flux tube expansion factor - solar wind speed relation with solar orbiter data . *Astronomy Astrophysics*, 691, A77. Retrieved from <https://doi.org/10.1051/0004-6361/202451272> doi: 10.1051/0004-6361/202451272
- Deb, K. (2001). *Multi-objective optimization using evolutionary algorithms*. Chichester: Wiley.
- de Pablos, D., Samanta, T., Badman, S. T., Schwanitz, C., Bahaouddin, S. M., Harra, L. K., ... Velli, M. (2022, July). Searching for a Solar Source of Magnetic-Field Switchbacks in Parker Solar Probe's First Encounter. *Solar Physics*, 297(7), 90. Retrieved from <https://doi.org/10.1007/s11207-022-02022-4> doi: 10.1007/s11207-022-02022-4
- Dierckx, P. (1975). An algorithm for smoothing, differentiation and integration of experimental data using spline functions. *Journal of Computational and Applied Mathematics*, 1(3), 165-184. Retrieved from <https://www.sciencedirect.com/science/article/pii/0771050X75900340> doi: [https://doi.org/10.1016/0771-050X\(75\)90034-0](https://doi.org/10.1016/0771-050X(75)90034-0)
- Ervin, T., Jaffarove, K., Badman, S. T., Huang, J., Rivera, Y. J., & Bale, S. D. (2024, November). Characteristics and Source Regions of Slow Alfvénic Solar Wind Observed by Parker Solar Probe. *The Astrophysical Journal*, 975(2), 21. Retrieved from <https://doi.org/10.3847/1538-4357/ad7d00> doi: 10.3847/1538-4357/ad7d00
- Evans, L. C. (2010). *Partial differential equations* (2nd ed., Vol. 19). Providence, Rhode Island: American Mathematical Society.
- Finley, A. J., & Brun, A. S. (2023). Accounting for differential rotation in calculations of the sun's angular momentum-loss rate. *Astronomy Astrophysics*, 674, A42. Retrieved from <https://doi.org/10.1051/0004-6361/202245642> doi: 10.1051/0004-6361/202245642

- Fox, N. J., Velli, M. C., Bale, S. D., Decker, R., Driesman, A., Howard, R. A., ... Szabo, A. (2016, December). The Solar Probe Plus Mission: Humanity's First Visit to Our Star. *Space Science Reviews*, 204(1), 7–48. Retrieved from <https://doi.org/10.1007/s11214-015-0211-6> doi: 10.1007/s11214-015-0211-6
- Habbal, S. R., Druckmüller, M., Alzate, N., Ding, A., Johnson, J., Starha, P., ... Arndt, M. (2021, apr). Identifying the coronal source regions of solar wind streams from total solar eclipse observations and in situ measurements extending over a solar cycle. *The Astrophysical Journal Letters*, 911(1), L4. Retrieved from <https://dx.doi.org/10.3847/2041-8213/abe775> doi: 10.3847/2041-8213/abe775
- Hahn, M., Bryans, P., Landi, E., Miralles, M. P., & Savin, D. W. (2010, nov). Properties of a polar coronal hole during the solar minimum in 2007. *The Astrophysical Journal*, 725(1), 774. Retrieved from <https://dx.doi.org/10.1088/0004-637X/725/1/774> doi: 10.1088/0004-637X/725/1/774
- Harris, C. R., Millman, K. J., van der Walt, S. J., Gommers, R., Virtanen, P., Cournapeau, D., ... Oliphant, T. E. (2020, September). Array programming with NumPy. *Nature*, 585(7825), 357–362. Retrieved from <https://doi.org/10.1038/s41586-020-2649-2> doi: 10.1038/s41586-020-2649-2
- Harvey, J. W., Hill, F., Hubbard, R. P., Kennedy, J. R., Leibacher, J. W., Pintar, J. A., ... Yasukawa, E. (1996). The global oscillation network group (gong) project. *Science*, 272(5266), 1284–1286. Retrieved from <https://www.science.org/doi/abs/10.1126/science.272.5266.1284> doi: 10.1126/science.272.5266.1284
- Hayashi, K., Yang, S., & Deng, Y. (2016). Comparison of potential field solutions for carrington rotation 2144. *Journal of Geophysical Research: Space Physics*, 121(2), 1046–1061. Retrieved from <https://agupubs.onlinelibrary.wiley.com/doi/abs/10.1002/2015JA021757> doi: <https://doi.org/10.1002/2015JA021757>
- Hoeksema, J. T., Wilcox, J. M., & Scherrer, P. H. (1983). The structure of the heliospheric current sheet: 1978–1982. *Journal of Geophysical Research: Space Physics*, 88(A12), 9910–9918. Retrieved from <https://agupubs.onlinelibrary.wiley.com/doi/abs/10.1029/JA088iA12p09910> doi: <https://doi.org/10.1029/JA088iA12p09910>
- Hou, C., He, J., Duan, D., Wu, Z., Chen, Y., Verscharen, D., ... Bale, S. D. (2024, October). The origin of interplanetary switchbacks in reconnection at chromospheric network boundaries. *Nature Astronomy*, 8(10), 1246–1256. Retrieved from <https://doi.org/10.1038/s41550-024-02321-9> doi: 10.1038/s41550-024-02321-9
- Huang, Z., Tóth, G., Huang, J., Sachdeva, N., van der Holst, B., & Manchester, W. B. (2024, apr). Adjusting the potential field source surface height based on magnetohydrodynamic simulations. *The Astrophysical Journal Letters*, 965(1), L1. Retrieved from <https://doi.org/10.3847/2041-8213/ad3547> doi: 10.3847/2041-8213/ad3547
- Hunter, J. D. (2007). Matplotlib: A 2d graphics environment. *Computing in Science & Engineering*, 9(3), 90–95. doi: 10.1109/MCSE.2007.55
- Ito, K., Kunisch, K., & Peichl, G. H. (2006). Variational approach to shape derivatives for a class of bernoulli problems. *Journal of Mathematical Analysis and Applications*, 314(1), 126–149. Retrieved from <https://www.sciencedirect.com/science/article/pii/S0022247X05002714> doi: <https://doi.org/10.1016/j.jmaa.2005.03.100>
- Ivanyshyn Yaman, O., & Kress, R. (2017). Nonlinear integral equations for bernoulli's free boundary value problem in three dimensions. *Computers and*

- Mathematics with Applications*, 74(11), 2784-2791. Retrieved from <https://www.sciencedirect.com/science/article/pii/S0898122117303590> (Proceedings of the International Conference on Computational Mathematics and Inverse Problems, On occasion of the 60th birthday of Prof. Peter Monk) doi: <https://doi.org/10.1016/j.camwa.2017.06.011>
- Kang, F., & Zhong-Ci, S. (1996). Finite element methods. In *Mathematical theory of elastic structures* (pp. 289–385). Berlin, Heidelberg: Springer Berlin Heidelberg. Retrieved from https://doi.org/10.1007/978-3-662-03286-2_5 doi: 10.1007/978-3-662-03286-2_5
- Karna, N., Hess Webber, S. A., & Pesnell, W. D. (2014, September). Using Polar Coronal Hole Area Measurements to Determine the Solar Polar Magnetic Field Reversal in Solar Cycle 24. *Solar Physics*, 289(9), 3381–3390. Retrieved from <https://doi.org/10.1007/s11207-014-0541-7> doi: 10.1007/s11207-014-0541-7
- Kasper, J. C., Abiad, R., Austin, G., Balat-Pichelin, M., Bale, S. D., Belcher, J. W., ... Zank, G. (2016, December). Solar Wind Electrons Alphas and Protons (SWEAP) Investigation: Design of the Solar Wind and Coronal Plasma Instrument Suite for Solar Probe Plus. *Space Science Reviews*, 204(1), 131–186. Retrieved from <https://doi.org/10.1007/s11214-015-0206-3> doi: 10.1007/s11214-015-0206-3
- Kawohl, B. (2019, September). Antoine Henrot, Michel Pierre “Shape Variation and Optimization, A Geometrical Analysis”. *Jahresbericht der Deutschen Mathematiker-Vereinigung*, 121(3), 239–241. Retrieved from <https://doi.org/10.1365/s13291-018-00195-1> doi: 10.1365/s13291-018-00195-1
- Koskela, J., Virtanen, I., & Mursula, K. (2019). Revisiting the coronal current sheet model: Parameter range analysis and comparison with the potential field model. *Astronomy Astrophysics*, 631, A17. Retrieved from <https://doi.org/10.1051/0004-6361/201935967> doi: 10.1051/0004-6361/201935967
- Koskela, J. S., Virtanen, I. I., & Mursula, K. (2018). Southward shift of the coronal neutral line and the heliospheric current sheet: Evidence for radial evolution of hemispheric asymmetry. *Astronomy Astrophysics*, 618, A105. Retrieved from <https://doi.org/10.1051/0004-6361/201832609> doi: 10.1051/0004-6361/201832609
- Koukras, A., Dolla, L., & Keppens, R. (2025). Estimating uncertainties in the back-mapping of the fast solar wind. *Astronomy Astrophysics*, 694, A134. Retrieved from <https://doi.org/10.1051/0004-6361/202244327> doi: 10.1051/0004-6361/202244327
- Kruse, M., Heidrich-Meisner, V., & Wimmer-Schweingruber, R. F. (2021). Evaluation of a potential field source surface model with elliptical source surfaces via ballistic back mapping of in situ spacecraft data. *Astronomy Astrophysics*, 645, A83. Retrieved from <https://doi.org/10.1051/0004-6361/202039120> doi: 10.1051/0004-6361/202039120
- Kruse, M., Heidrich-Meisner, V., Wimmer-Schweingruber, R. F., & Hauptmann, M. (2020). An elliptic expansion of the potential field source surface model. *Astronomy Astrophysics*, 638, A109. Retrieved from <https://doi.org/10.1051/0004-6361/202037734> doi: 10.1051/0004-6361/202037734
- Lee, C. O., Luhmann, J. G., Hoeksema, J. T., Sun, X., Arge, C. N., & de Pater, I. (2011, April). Coronal Field Opens at Lower Height During the Solar Cycles 22 and 23 Minimum Periods: IMF Comparison Suggests the Source Surface Should Be Lowered. *Solar Physics*, 269(2), 367–388. Retrieved from <https://doi.org/10.1007/s11207-010-9699-9> doi: 10.1007/s11207-010-9699-9

- Levine, R. H., Schulz, M., & Frazier, E. N. (1982, April). Simulation of the magnetic structure of the inner heliosphere by means of a non-spherical source surface. *Solar Physics*, 77(1), 363–392. Retrieved from <https://doi.org/10.1007/BF00156118> doi: 10.1007/BF00156118
- Li, H., Feng, X., & Wei, F. (2021). Comparison of synoptic maps and pfss solutions for the declining phase of solar cycle 24. *Journal of Geophysical Research: Space Physics*, 126(3), e2020JA028870. Retrieved from <https://agupubs.onlinelibrary.wiley.com/doi/abs/10.1029/2020JA028870> (e2020JA028870 2020JA028870) doi: <https://doi.org/10.1029/2020JA028870>
- Lieberman, G. M. (1986). Mixed boundary value problems for elliptic and parabolic differential equations of second order. *Journal of Mathematical Analysis and Applications*, 113(2), 422–440. Retrieved from <https://www.sciencedirect.com/science/article/pii/0022247X86903148> doi: [https://doi.org/10.1016/0022-247X\(86\)90314-8](https://doi.org/10.1016/0022-247X(86)90314-8)
- Lin, R., Luo, Z., He, J., Xie, L., Hou, C., & Chen, S. (2024). Prediction of solar wind speed through machine learning from extrapolated solar coronal magnetic field. *Space Weather*, 22(6), e2023SW003561. Retrieved from <https://agupubs.onlinelibrary.wiley.com/doi/abs/10.1029/2023SW003561> (e2023SW003561 2023SW003561) doi: <https://doi.org/10.1029/2023SW003561>
- Linker, J. A., Caplan, R. M., Downs, C., Riley, P., Mikic, Z., Lionello, R., ... Owens, M. J. (2017, oct). The open flux problem. *The Astrophysical Journal*, 848(1), 70. Retrieved from <https://dx.doi.org/10.3847/1538-4357/aa8a70> doi: 10.3847/1538-4357/aa8a70
- Linker, J. A., Heinemann, S. G., Temmer, M., Owens, M. J., Caplan, R. M., Arge, C. N., ... Vrsnak, B. (2021, aug). Coronal hole detection and open magnetic flux. *The Astrophysical Journal*, 918(1), 21. Retrieved from <https://dx.doi.org/10.3847/1538-4357/ac090a> doi: 10.3847/1538-4357/ac090a
- Liu, X., Feng, X., Lv, J., Wang, X., & Zhang, M. (2022). Direct discontinuous galerkin method for potential magnetic field solutions. *Frontiers in Astronomy and Space Sciences*, 9. Retrieved from <https://www.frontiersin.org/journals/astronomy-and-space-sciences/articles/10.3389/fspas.2022.1055969> doi: 10.3389/fspas.2022.1055969
- Liu, Y., Shen, F., & Yang, Y. (2019, dec). Numerical simulation on the propagation and deflection of fast coronal mass ejections (cmes) interacting with a corotating interaction region in interplanetary space. *The Astrophysical Journal*, 887(2), 150. Retrieved from <https://dx.doi.org/10.3847/1538-4357/ab543e> doi: 10.3847/1538-4357/ab543e
- Livi, R., Larson, D. E., Kasper, J. C., Abiad, R., Case, A. W., Klein, K. G., ... McManus, M. D. (2022, oct). The solar probe analyzer—ions on the parker solar probe. *The Astrophysical Journal*, 938(2), 138. Retrieved from <https://doi.org/10.3847/1538-4357/ac93f5> doi: 10.3847/1538-4357/ac93f5
- Lowder, C., Qiu, J., Leamon, R., & Liu, Y. (2014, feb). Measurements of euv coronal holes and open magnetic flux. *The Astrophysical Journal*, 783(2), 142. Retrieved from <https://dx.doi.org/10.1088/0004-637X/783/2/142> doi: 10.1088/0004-637X/783/2/142
- Miettinen, K. M. (1999). *Nonlinear multiobjective optimization* (Vol. 12). Dordrecht: Kluwer Academic Publishers.
- Müller, D., St. Cyr, O. C., Zouganelis, I., Gilbert, H. R., Marsden, R., Nieves-Chinchilla, T., ... Williams, D. (2022). Reconstructing solar magnetic fields from historical ob-

- servations - ix. the photospheric magnetic field from 1915 to 1985. *Astronomy and Astrophysics*, 667, A168. Retrieved from <https://doi.org/10.1051/0004-6361/202244372> doi: 10.1051/0004-6361/202244372
- Nikolic, L. (2019). On solutions of the pfss model with gong synoptic maps for 2006–2018. *Space Weather*, 17(8), 1293–1311. Retrieved from <https://agupubs.onlinelibrary.wiley.com/doi/abs/10.1029/2019SW002205> doi: <https://doi.org/10.1029/2019SW002205>
- Nolte, J. T., & Roelof, E. C. (1973, November). Large-Scale Structure of the Interplanetary Medium, I: High Coronal Source Longitude of the Quiet-Time Solar Wind. *Solar Physics*, 33(1), 241–257. doi: 10.1007/BF00152395
- Nurbekyan, L., Lei, W., & Yang, Y. (2022). Efficient natural gradient descent methods for large-scale optimization problems. *ArXiv, abs/2202.06236*. Retrieved from <https://api.semanticscholar.org/CorpusID:246823871>
- Panasenco, O., Velli, M., D’Amicis, R., Shi, C., Réville, V., Bale, S. D., ... Whitteley, P. (2020, feb). Exploring solar wind origins and connecting plasma flows from the parker solar probe to 1 au: Nonspherical source surface and alfvénic fluctuations. *The Astrophysical Journal Supplement Series*, 246(2), 54. Retrieved from <https://dx.doi.org/10.3847/1538-4365/ab61f4> doi: 10.3847/1538-4365/ab61f4
- Park, J., Bucik, R., Jeong, H.-J., & Moon, Y.-J. (2024, dec). Fe/o variations relative to source longitude and heliospheric current sheet in large solar energetic particle events. *The Astrophysical Journal*, 977(1), 86. Retrieved from <https://dx.doi.org/10.3847/1538-4357/ad843e> doi: 10.3847/1538-4357/ad843e
- Parker, E. N. (1958, November). Dynamics of the Interplanetary Gas and Magnetic Fields. *The Astrophysical Journal*, 128, 664. doi: 10.1086/146579
- Pesnell, W. D., Thompson, B. J., & Chamberlin, P. C. (2012, January). The Solar Dynamics Observatory (SDO). *Solar Physics*, 275(1), 3–15. Retrieved from <https://doi.org/10.1007/s11207-011-9841-3> doi: 10.1007/s11207-011-9841-3
- Pishkalo, M. I. (2019, October). On Polar Magnetic Field Reversal in Solar Cycles 21, 22, 23, and 24. *Solar Physics*, 294(10), 137. Retrieved from <https://doi.org/10.1007/s11207-019-1520-9> doi: 10.1007/s11207-019-1520-9
- Poduval, B., & Zhao, X. P. (2004). Discrepancies in the prediction of solar wind using potential field source surface model: An investigation of possible sources. *Journal of Geophysical Research: Space Physics*, 109(A8). Retrieved from <https://agupubs.onlinelibrary.wiley.com/doi/abs/10.1029/2004JA010384> doi: <https://doi.org/10.1029/2004JA010384>
- Rabago, J. F. T., & Azegami, H. (2019, September). A new energy-gap cost functional approach for the exterior bernoulli free boundary problem. *Evolution Equations and Control Theory*, 8(4), 785–824. Retrieved from <https://www.aims sciences.org/article/id/712cbcaa-14f7-44f3-b062-d4072ec7d941> doi: 10.3934/eect.2019038
- Rabago, J. F. T., & Azegami, H. (2020, September). A second-order shape optimization algorithm for solving the exterior Bernoulli free boundary problem using a new boundary cost functional. *Computational Optimization and Applications*, 77(1), 251–305. Retrieved from <https://doi.org/10.1007/s10589-020-00199-7> doi: 10.1007/s10589-020-00199-7
- Raissi, M., Perdikaris, P., & Karniadakis, G. (2019). Physics-informed neural networks: A deep learning framework for solving forward and inverse problems involving nonlinear partial differential equations. *Journal of Computational Physics*, 378,

- 686-707. Retrieved from <https://www.sciencedirect.com/science/article/pii/S0021999118307125> doi: <https://doi.org/10.1016/j.jcp.2018.10.045>
- Raouafi, N. E., Matteini, L., Squire, J., Badman, S. T., Velli, M., Klein, K. G., ... Woolley, T. (2023, February). Parker Solar Probe: Four Years of Discoveries at Solar Cycle Minimum. *Space Science Reviews*, *219*(1), 8. Retrieved from <https://doi.org/10.1007/s11214-023-00952-4> doi: 10.1007/s11214-023-00952-4
- Romeo, O. M., Braga, C. R., Badman, S. T., Larson, D. E., Stevens, M. L., Huang, J., ... Linton, M. G. (2023, sep). Near-sun in situ and remote-sensing observations of a coronal mass ejection and its effect on the heliospheric current sheet. *The Astrophysical Journal*, *954*(2), 168. Retrieved from <https://dx.doi.org/10.3847/1538-4357/ace62e> doi: 10.3847/1538-4357/ace62e
- Schatten, K. H., Wilcox, J. M., & Ness, N. F. (1969, March). A model of interplanetary and coronal magnetic fields. *Solar Physics*, *6*(3), 442–455. Retrieved from <https://doi.org/10.1007/BF00146478> doi: 10.1007/BF00146478
- Scherrer, P. H., Schou, J., Bush, R. I., Kosovichev, A. G., Bogart, R. S., Hoeksema, J. T., ... Tomczyk, S. (2012, January). The Helioseismic and Magnetic Imager (HMI) Investigation for the Solar Dynamics Observatory (SDO). *Solar Physics*, *275*(1), 207–227. Retrieved from <https://doi.org/10.1007/s11207-011-9834-2> doi: 10.1007/s11207-011-9834-2
- Schrijver, C. J., Derosa, M. L., Metcalf, T. R., Liu, Y., Mctiernan, J., Régnier, S., ... Wiegmann, T. (2006, May). Nonlinear Force-Free Modeling of Coronal Magnetic Fields Part I: A Quantitative Comparison of Methods. *Solar Physics*, *235*(1), 161–190. Retrieved from <https://doi.org/10.1007/s11207-006-0068-7> doi: 10.1007/s11207-006-0068-7
- Schulz, M. (1997). Non-spherical source-surface model of the heliosphere: a scalar formulation. *Annales Geophysicae*, *15*(11), 1379–1387. Retrieved from <https://angeo.copernicus.org/articles/15/1379/1997/> doi: 10.1007/s00585-997-1379-1
- Schulz, M., Frazier, E. N., & Boucher, D. J. (1978, November). Coronal magnetic-field model with non-spherical source surface. *Solar Physics*, *60*(1), 83–104. Retrieved from <https://doi.org/10.1007/BF00152334> doi: 10.1007/BF00152334
- Shen, F., Feng, X., Wu, S. T., & Xiang, C. (2007). Three-dimensional mhd simulation of cmes in three-dimensional background solar wind with the self-consistent structure on the source surface as input: Numerical simulation of the january 1997 sun-earth connection event. *Journal of Geophysical Research: Space Physics*, *112*(A6). Retrieved from <https://agupubs.onlinelibrary.wiley.com/doi/abs/10.1029/2006JA012164> doi: <https://doi.org/10.1029/2006JA012164>
- Shen, F., Feng, X., & Xiang, C. (2012). Improvement to the global distribution of coronal plasma and magnetic field on the source surface using expansion factor f_s and angular distance θ_{tab} . *Journal of Atmospheric and Solar-Terrestrial Physics*, *77*, 125-131. Retrieved from <https://www.sciencedirect.com/science/article/pii/S1364682611003427> doi: <https://doi.org/10.1016/j.jastp.2011.12.009>
- Shen, F., Feng, X., Xiang, C., & Song, W. (2010). The statistical and numerical study of the global distribution of coronal plasma and magnetic field near 2.5rs over a 10-year period. *Journal of Atmospheric and Solar-Terrestrial Physics*, *72*(13), 1008-1018. Retrieved from <https://www.sciencedirect.com/science/article/pii/S1364682610001604> doi: <https://doi.org/10.1016/j.jastp.2010.05.016>
- Shen, F., Feng, X. S., Wang, Y., Wu, S. T., Song, W. B., Guo, J. P., & Zhou, Y. F. (2011). Three-dimensional mhd simulation of two coronal mass ejections' propagation and interaction using a successive magnetized plasma blobs model.

- Journal of Geophysical Research: Space Physics*, 116(A9). Retrieved from <https://agupubs.onlinelibrary.wiley.com/doi/abs/10.1029/2011JA016584>
doi: <https://doi.org/10.1029/2011JA016584>
- Shen, F., Feng, X. S., Wu, S. T., Xiang, C. Q., & Song, W. B. (2011). Three-dimensional mhd simulation of the evolution of the april 2000 cme event and its induced shocks using a magnetized plasma blob model. *Journal of Geophysical Research: Space Physics*, 116(A4). Retrieved from <https://agupubs.onlinelibrary.wiley.com/doi/abs/10.1029/2010JA015809> doi: <https://doi.org/10.1029/2010JA015809>
- Shen, F., Yang, Z., Zhang, J., Wei, W., & Feng, X. (2018, oct). Three-dimensional mhd simulation of solar wind using a new boundary treatment: Comparison with in situ data at earth. *The Astrophysical Journal*, 866(1), 18. Retrieved from <https://dx.doi.org/10.3847/1538-4357/aad806> doi: [10.3847/1538-4357/aad806](https://doi.org/10.3847/1538-4357/aad806)
- Smith, E. J., & Balogh, A. (1995). Ulysses observations of the radial magnetic field. *Geophysical Research Letters*, 22(23), 3317-3320. Retrieved from <https://agupubs.onlinelibrary.wiley.com/doi/abs/10.1029/95GL02826> doi: <https://doi.org/10.1029/95GL02826>
- Smith, E. J., & Balogh, A. (2003, September). Open Magnetic Flux: Variation with Latitude and Solar Cycle. *AIP Conference Proceedings*, 679(1), 67-70. Retrieved from <https://doi.org/10.1063/1.1618543> (eprint: https://pubs.aip.org/aip/acp/article-pdf/679/1/67/11484523/67_1_online.pdf)
doi: [10.1063/1.1618543](https://doi.org/10.1063/1.1618543)
- Sokolowski, J., & Zolesio, J.-P. (1992). Shape sensitivity analysis of variational inequalities. In *Introduction to shape optimization: Shape sensitivity analysis* (pp. 163-239). Berlin, Heidelberg: Springer Berlin Heidelberg. Retrieved from https://doi.org/10.1007/978-3-642-58106-9_4 doi: [10.1007/978-3-642-58106-9_4](https://doi.org/10.1007/978-3-642-58106-9_4)
- Song, L., Tan, Y., Yu, F., Luo, Y., & Zheng, J. (2024, October). Optimal approximations for the free boundary problems of the space-time fractional Black-Scholes equations using a combined physics-informed neural network. *Scientific Reports*, 14(1), 25289. Retrieved from <https://doi.org/10.1038/s41598-024-77073-7> doi: [10.1038/s41598-024-77073-7](https://doi.org/10.1038/s41598-024-77073-7)
- Stansby, D., & Verscharen, D. (2022). *Test problems for potential field source surface extrapolations of solar and stellar magnetic fields*. Retrieved from <https://arxiv.org/abs/2201.07783>
- Stone, E., Frandsen, A., Mewaldt, R., Christian, E., Margolies, D., Ormes, J., & Snow, F. (1998, July). The Advanced Composition Explorer. *Space Science Reviews*, 86(1), 1-22. Retrieved from <https://doi.org/10.1023/A:1005082526237> doi: [10.1023/A:1005082526237](https://doi.org/10.1023/A:1005082526237)
- Strauss, W. A. (2008). *Partial differential equations: An introduction* (2nd ed.). Hoboken, New Jersey: Wiley.
- Tepper, D. E. (1975). On a free boundary problem, the starlike case. *SIAM Journal on Mathematical Analysis*, 6(3), 503-505. Retrieved from <https://doi.org/10.1137/0506045> doi: [10.1137/0506045](https://doi.org/10.1137/0506045)
- The SunPy Community, Barnes, W. T., Bobra, M. G., Christe, S. D., Freij, N., Hayes, L. A., ... Dang, T. K. (2020). The sunpy project: Open source development and status of the version 1.0 core package. *The Astrophysical Journal*, 890, 68-. Retrieved from <https://iopscience.iop.org/article/10.3847/1538-4357/ab4f7a> doi: [10.3847/1538-4357/ab4f7a](https://doi.org/10.3847/1538-4357/ab4f7a)
- Toth, G., van der Holst, B., & Huang, Z. (2011, apr). Obtaining potential field solutions with spherical harmonics and finite differences. *The Astrophysical Journal*, 732(2),

102. Retrieved from <https://doi.org/10.1088/0004-637X/732/2/102> doi: 10.1088/0004-637X/732/2/102
- Tukey, J. W. (1977). *Exploratory data analysis*. Reading, MA: Addison-Wesley.
- Tähtinen, I., Asikainen, T., & Mursula, K. (2024). Straight outta photosphere: Open solar flux without coronal modeling. *Astronomy Astrophysics*, 688, L32. Retrieved from <https://doi.org/10.1051/0004-6361/202451267> doi: 10.1051/0004-6361/202451267
- Virtanen, I., & Mursula, K. (2019). Photospheric and coronal magnetic fields in six magnetographs - iii. photospheric and coronal magnetic fields in 1974–2017. *Astronomy Astrophysics*, 626, A67. Retrieved from <https://doi.org/10.1051/0004-6361/201935713> doi: 10.1051/0004-6361/201935713
- Virtanen, I. O. I., Pevtsov, A. A., Bertello, L., & Mursula, K. (2022). Reconstructing solar magnetic fields from historical observations - ix. the photospheric magnetic field from 1915 to 1985. *Astronomy Astrophysics*, 667, A168. Retrieved from <https://doi.org/10.1051/0004-6361/202244372> doi: 10.1051/0004-6361/202244372
- Virtanen, P., Gommers, R., Oliphant, T. E., Haberland, M., Reddy, T., Cournapeau, D., ... SciPy 1.0 Contributors (2020). SciPy 1.0: Fundamental Algorithms for Scientific Computing in Python. *Nature Methods*, 17, 261–272. doi: 10.1038/s41592-019-0686-2
- Wang, S. (2025, September). *Optimization algorithm for determining the source surface radius based on parker solar probe in-situ measurements: Encounters 1-19*. [Dataset]. Zenodo. Retrieved from <https://doi.org/10.5281/zenodo.17129425> doi: 10.5281/zenodo.17129425
- Wang, X., Su, J., & Zhang, H. (2010). Calibration of a full-disc longitudinal magnetogram at the huairou solar observing station. *Monthly Notices of the Royal Astronomical Society*, 406(2), 1166–1176. Retrieved from <https://onlinelibrary.wiley.com/doi/abs/10.1111/j.1365-2966.2010.16745.x> doi: <https://doi.org/10.1111/j.1365-2966.2010.16745.x>
- Wang, Y.-M., Robbrecht, E., & Sheeley, N. R. (2009, dec). On the weakening of the polar magnetic fields during solar cycle 23. *The Astrophysical Journal*, 707(2), 1372. Retrieved from <https://dx.doi.org/10.1088/0004-637X/707/2/1372> doi: 10.1088/0004-637X/707/2/1372
- Wei, W., Shen, F., Yang, Z., Zhao, L., Wang, Y., Zuo, P., & Zhang, J. (2019). Modeling solar energetic particle transport in 3d background solar wind: Influences of the compression regions. *Journal of Atmospheric and Solar-Terrestrial Physics*, 182, 155–164. Retrieved from <https://www.sciencedirect.com/science/article/pii/S1364682618304243> doi: <https://doi.org/10.1016/j.jastp.2018.11.012>
- Yalim, M. S., Pogorelov, N., & Liu, Y. (2017, may). A data-driven mhd model of the global solar corona within multi-scale fluid-kinetic simulation suite (ms-flukss). *Journal of Physics: Conference Series*, 837(1), 012015. Retrieved from <https://dx.doi.org/10.1088/1742-6596/837/1/012015> doi: 10.1088/1742-6596/837/1/012015
- Yang, S., Jiang, J., Wang, Z., Hou, Y., Jin, C., Song, Q., ... Wang, J. (2024a, jul). Long-term variation of the solar polar magnetic fields at different latitudes. *Research in Astronomy and Astrophysics*, 24(7), 075015. Retrieved from <https://dx.doi.org/10.1088/1674-4527/ad539a> doi: 10.1088/1674-4527/ad539a
- Yang, S., Jiang, J., Wang, Z., Hou, Y., Jin, C., Song, Q., ... Wang, J. (2024b, jul). Long-term variation of the solar polar magnetic fields at different latitudes. *Research in Astronomy and Astrophysics*, 24(7), 075015. Retrieved from <https://>

- [dx.doi.org/10.1088/1674-4527/ad539a](https://doi.org/10.1088/1674-4527/ad539a) doi: 10.1088/1674-4527/ad539a
- Yang, Y., & Shen, F. (2019, August). Modeling the Global Distribution of Solar Wind Parameters on the Source Surface Using Multiple Observations and the Artificial Neural Network Technique. *Solar Physics*, 294(8), 111. Retrieved from <https://doi.org/10.1007/s11207-019-1496-5> doi: 10.1007/s11207-019-1496-5
- Yang, Y., Shen, F., Yang, Z., & Feng, X. (2018). Prediction of solar wind speed at 1 au using an artificial neural network. *Space Weather*, 16(9), 1227-1244. Retrieved from <https://agupubs.onlinelibrary.wiley.com/doi/abs/10.1029/2018SW001955> doi: <https://doi.org/10.1029/2018SW001955>
- Zhao, J., Wang, S., Sun, W., Zhu, X., Hou, C., Zong, Q., ... Yang, L. (2025, feb). Statistics of the interplanetary magnetic field from 0.1 to 30 au. i. distribution character. *The Astrophysical Journal*, 980(1), 89. Retrieved from <https://dx.doi.org/10.3847/1538-4357/ad9b28> doi: 10.3847/1538-4357/ad9b28
- Zhao, L., & Zhang, M. (2018, jun). Effects of coronal magnetic field structures on the transport of solar energetic particles. *The Astrophysical Journal Letters*, 859(2), L29. Retrieved from <https://dx.doi.org/10.3847/2041-8213/aac6cf> doi: 10.3847/2041-8213/aac6cf
- Zhu, Y., & Shen, F. (2024). Solar energetic particles propagation under 3d corotating interaction regions with different characteristic parameters. *Universe*, 10(8). Retrieved from <https://www.mdpi.com/2218-1997/10/8/315> doi: 10.3390/universe10080315

Appendix A Magnetic Field at Source Surface and PSP in situ Measurements

Figure S1 in Supporting Information shows the solution of Eq.A1 at the source surface. Table S1 lists the Carrington rotation magnetograms used for PSP Encounters 1-19. The vertical axis gives colatitude and the horizontal axis gives longitude. We follow the spherical harmonic implementation described in Xudong Sun's notes, available at <http://wso.stanford.edu/words/pfss.pdf>. Equations (10), (16), (17), and (18) in those notes contain errors. The magnetic potential series must start from the zeroth harmonic term, $L = 0$, and the magnetic field series must start from the first harmonic term, $L = 1$. The forward problem for PFSS extrapolation is

$$\begin{cases} -\Delta\psi = 0 & \text{in } \Omega, \\ \partial_{\mathbf{n}}\psi = B_r(\gamma) & \text{on } \Gamma, \\ \psi = 0 & \text{on } \Sigma. \end{cases} \quad (\text{A1})$$

This mixed boundary elliptic PDE can be solved by separation of variables. For a spherical source surface, the solution of the PFSS extrapolation has the analytic expansion

$$\psi(r, \theta, \phi) = R_s \sum_{l=0}^{\infty} \sum_{m=0}^l P_l^m(\cos(\theta)) (g_l^m \cos(m\phi) + h_l^m \sin(m\phi)) \left[c_l \left(\frac{R_s}{r}\right)^{l+1} - d_l \left(\frac{r}{R_s}\right)^l \right], \quad (\text{A2})$$

where c_l, d_l are given by

$$c_l = \frac{(R_{ss})^{2l+1}}{(l+1)(R_{ss})^{2l+1} + l(R_s)^{2l+1}}, \quad d_l = \frac{(R_s)^{2l+1}}{(l+1)(R_{ss})^{2l+1} + l(R_s)^{2l+1}}. \quad (\text{A3})$$

The magnetic field is defined by $\mathbf{B} = -\nabla\psi$, and the coefficients g_l^m, h_l^m are projected on the triangular basis functions

$$B_r(\gamma) = \sum_{l=1}^{\infty} \sum_{m=0}^l P_l^m(\cos(\theta)) (g_l^m \cos(m\phi) + h_l^m \sin(m\phi)) [(l+1)c_l + ld_l], \quad (\text{A4})$$

$$\int_{\Gamma} B_r(\gamma) H_l^m(\gamma) d\Gamma = \begin{cases} 2\pi & m = 0, \\ \pi & m \neq 0, \end{cases} \quad (\text{A5})$$

where $H_l^m(\gamma) = P_l^m(\cos(\theta)) \cos m\phi$, the associated Legendre functions $P_l^m(x)$ are normalized with the coefficients

$$A_l^m = \sqrt{\frac{2l+1}{2} \frac{(l-m)!}{(l+m)!}}, \quad \int_{-1}^1 |A_l^m P_l^m(x)|^2 dx = 1. \quad (\text{A6})$$

We process the radial solar wind velocity and radial magnetic field from PSP in situ measurements with first order linear interpolation and the IQR method, respectively. Figure S2 in Supporting Information exhibits the processed results for each encounter, with the left vertical axis of each subplot quantifying the radial solar wind velocity (km/s) and the right vertical axis representing the radial magnetic field magnitude (nT). This dual axis visualization enables simultaneous analysis of velocity and magnetic field correlations across distinct encounters. The subplots reveals that the observed polarity inversions exhibit correlations with captured high velocity streams during Encounters 11, 13-17. This association suggests that the ascending phases of solar activity influences the iteration of R_{ss} within optimization frameworks.

Appendix B Parker Spiral Lines and Reference Simulations

Parker spiral lines are defined by the following mapping

$$\frac{dr}{v_{sw}} = \frac{d\phi}{\omega_s}, \quad (\text{B1})$$

where v_{sw} is radial solar wind velocity, and ω_s denotes the angular velocity of rotation near the solar equator. The Parker spiral angle $\phi(r)$ at heliocentric distance is formulated by

$$\phi(r) = \phi_0 - \frac{\omega_s}{v_{sw}}(r - r_0), \quad (\text{B2})$$

where ϕ_0, r_0 represent the initial position of Parker spiral lines, usually defined by the location of PSP. We then derive the Parker ballistic backmapping from PSP in situ measurements to the source surface using Eq.B2

$$\tilde{\mathcal{P}} \rightarrow \tilde{\mathcal{Q}}, \quad (r_{\text{PSP}}, \theta_{\text{PSP}}, \phi_{\text{PSP}}) \mapsto \left(R_{ss}, \theta_{\text{PSP}}, \phi_{\text{PSP}} - \frac{\omega_s}{v_{sw}}(R_{ss} - r_{\text{PSP}}) \right), \quad (\text{B3})$$

and the magnetic field backmapping is defined as

$$\begin{cases} B_r(\tilde{\mathcal{P}}) = \left(\frac{R_{ss}}{r_{\text{PSP}}} \right)^2 B_r(\tilde{\mathcal{Q}}), \\ B_\theta(\tilde{\mathcal{P}}) = 0 \\ B_\phi(\tilde{\mathcal{P}}) = \left(\frac{\omega_s}{v_{sw}} \right) (r_{\text{PSP}} - R_{ss}) \sin(\theta) B_r(\tilde{\mathcal{P}}). \end{cases} \quad (\text{B4})$$

To illustrate the two inputs to the objective functional, we run reference PFSS extrapolations with $R_{ss} = 2.0R_s$ and $2.5R_s$ for PSP Encounters 1-19 and extract the corresponding B_r^k time series. Figure S3 in Supporting Information shows these results for the 19 Carrington rotations. Red and blue markers denote the measured radial magnetic field, and black and orange markers denote the two fixed R_{ss} reference solutions. Figure S1 in Supporting Information shows the corresponding source surface field distributions.

We use Table S2 to compare the magnetic field scaling factor, the normalized objective functional, the supplementary rescaled objective values reported in the table, and the polarity prediction accuracy for the reference solutions. Because the magnetic field amplitude changes strongly from one encounter to another, we normalize the objective functional separately for each encounter using the encounter mean μ^k and standard deviation σ^k . This normalization allows a consistent comparison across PSP encounters.

The scaling factors satisfy $\alpha^k > 1$ throughout Table S2, which reflects the familiar underestimation of open flux by PFSS extrapolation. Lowering R_{ss} increases the amount of magnetic flux treated as open under the boundary condition used in the PFSS extrapolation, so the $R_{ss} = 2.0R_s$ reference case generally gives smaller scaling factors than the $R_{ss} = 2.5R_s$ case. The scaling factors also tend to decrease from the early encounters to the later ones, which is consistent with the improvement seen during the ascending phase in both PSP and ACE comparisons.

Table S3 shows the corresponding ACE comparisons. The polarity prediction accuracy is generally higher during the ascending phase, and the objective functional shows the same broad trend. Because polarity prediction accuracy is not continuously differentiable, we do not use it as the single objective in Algorithm 1. We instead use the

normalized objective functional as the optimization target and reserve the scaling factor, white light image comparisons, and coronal hole area fractions for evaluation and interpretation.

Appendix C Argument

C1 Lemma 2.1

The proof of lemma 2.1 is shown below.

Proof. Necessity follows directly from integration by parts. Taking an arbitrary $\phi \in V(\Omega)$, multiply the Laplace equation $-\Delta\psi = 0$ with ϕ and integrate to obtain

$$\int_{\Omega} (-\Delta\psi) \phi \, dx = 0, \quad (\text{C1})$$

where $(-\Delta\psi) \phi \in L^1(\Omega)$ by Cauchy Schwarz inequality:

$$\|(\Delta\psi) \phi\|_{L^1(\Omega)} \leq \|\Delta\psi\|_{L^2(\Omega)} \|\phi\|_{L^2(\Omega)}. \quad (\text{C2})$$

Applying integration by parts to (C1) leads to the variational form

$$\begin{aligned} \int_{\Omega} (-\Delta\psi) \phi \, dx &= \sum_{i=1}^3 \int_{\Omega} (-\partial_i \partial_i \psi) \phi \, dx \\ &= \sum_{i=1}^3 \left(- \int_{\partial\Omega} (\gamma_0(\partial_i \psi) \cdot n_i) \gamma_0(\phi) \, d\sigma + \int_{\Omega} (\partial_i \psi) (\partial_i \phi) \, dx \right) \\ &= - \int_{\Sigma \cup \Gamma} \gamma_0(\phi) \gamma_0(\nabla\psi) \cdot \mathbf{n} \, d\sigma + \int_{\Omega} (\nabla\psi) \cdot (\nabla\phi) \, dx \\ &= - \int_{\Gamma} \gamma_0(\phi) g \, d\sigma + \int_{\Omega} (\nabla\psi) \cdot (\nabla\phi) \, dx \\ &= 0, \end{aligned} \quad (\text{C3})$$

where the index i represents the i th component subspace of \mathbb{R}^3 . From (C3), we prove to the necessity.

Conversely, if there exists $\psi \in V(\Omega)$ such that

$$\int_{\Omega} (\nabla\psi) \cdot (\nabla\phi) \, dx = \int_{\Gamma} g \gamma_0(\phi) \, d\sigma, \quad \forall \phi \in V(\Omega). \quad (\text{C4})$$

Hence, if $\phi \in \mathcal{D}(\Omega) := \{v \in V : \partial_i v \in L^2_{loc}(\Omega)\}$,

$$\begin{aligned} \int_{\Omega} (\nabla\psi) \cdot (\nabla\phi) \, dx &= \int_{\Gamma} g \gamma_0(\phi) \, d\sigma \\ &= 0, \quad \forall \phi \in \mathcal{D}(\Omega). \end{aligned} \quad (\text{C5})$$

We conclude that $\Delta\psi = 0$, $\psi \in V(\Omega)$. Now we prove that ψ satisfies the boundary conditions on Γ and Σ . It is evident that the boundary conditions hold on Σ due to $\psi \in V(\Omega)$. By integrating the left hand side of (7) by parts, we obtain:

$$\int_{\Gamma} \gamma_0(\phi) \gamma_0(\nabla\psi) \cdot \mathbf{n} \, d\sigma - \int_{\Omega} (\Delta\psi) \phi \, dx = \int_{\Gamma} g \gamma_0(\phi) \, d\sigma, \quad \forall \phi \in V(\Omega). \quad (\text{C6})$$

Then $\Delta\psi$ vanishes, simplifying formula (C6) to

$$\int_{\Gamma} \gamma_0(\phi) (\gamma_0(\nabla\psi) \cdot \mathbf{n} - g) \, d\sigma = 0, \quad \forall \phi \in V(\Omega). \quad (\text{C7})$$

Selecting a suitable $\psi \in V(\Omega)$ such that $\gamma_0(\psi) = \gamma_0(\nabla\psi) \cdot \mathbf{n} - g$, we obtain

$$\int_{\Gamma} (\gamma_0(\nabla\psi) \cdot \mathbf{n} - g)^2 \, d\sigma = 0. \quad (\text{C8})$$

That implies $\partial_{\mathbf{n}}\psi|_{\Gamma} = g$. □

C2 The Proof of Theorem 2.1

The proof of theorem 2.1 is shown below.

Proof. We first demonstrate the V -elliptic property of $a(\cdot, \cdot)$ via the Poincaré inequality

$$\begin{aligned} a(\phi, \phi) &= \int_{\Omega} |\nabla\psi|^2 \, dx \\ &= \|\nabla\psi\|_{L^2(\Omega)}^2 \geq C^2 \|\psi\|_{V(\Omega)}^2, \quad \forall \phi \in V(\Omega). \end{aligned} \quad (\text{C9})$$

Hence, $a(\cdot, \cdot)$ is V -elliptic with coefficient $\alpha := C^{-2}$. The continuity of $a(\cdot, \cdot)$ follows directly from the Cauchy Schwarz inequality:

$$\begin{aligned} |a(\psi, \phi)| &= \left| \int_{\Omega} (\nabla\psi) \cdot (\nabla\phi) \, dx \right| \\ &\leq \|\nabla\psi\|_{L^2(\Omega)} \cdot \|\nabla\phi\|_{L^2(\Omega)} \\ &\leq \|\nabla\psi\|_{V(\Omega)} \cdot \|\nabla\phi\|_{V(\Omega)}, \quad \forall (\psi, \phi) \in V \times V. \end{aligned} \quad (\text{C10})$$

Similarly, the continuity of $\eta_g(\phi)$ is established by the trace theorem:

$$\begin{aligned} |\eta_g(\phi)| &= \left| \int_{\Gamma} g\gamma_0(\phi) \, dx \right| \\ &\leq \|g\|_{L^2(\Gamma)} \cdot \|\gamma_0(\phi)\|_{L^2(\Gamma)} \\ &\leq \tilde{C} \|g\|_{L^2(\Gamma)} \cdot \|\phi\|_{V(\Omega)}, \quad \forall \phi \in V(\Omega). \end{aligned} \quad (\text{C11})$$

Hence, $a(\cdot, \cdot)$ and $\eta_g(\cdot)$ satisfy the conditions of the Lax-Milgram theorem. That proves existence and uniqueness of the solution for PFSS extrapolation in $V(\Omega)$. □

C3 The Proof of Lemma 2.2

The proof of lemma 2.2 is shown below.

Proof. The homeomorphic mappings φ_n satisfy uniform boundedness and equicontinuity, implying \mathcal{P} is weakly compact by the Arzelà-Ascoli theorem. Hence, any sequence in \mathcal{P} admits a convergent subsequence $\varphi_{n_k} \rightarrow \varphi$. The convergence of parameterized domains φ_n follows from the weak compactness of \mathcal{P} .

The last two sequences are convergent due to the boundedness of (12) and estimations on the variational equations. The variational equations for two auxiliary problems are

$$\text{find } \psi_{D_{n_k}} \in V(\Omega_{n_k}), \text{ such that: } \int_{\Omega_{n_k}} \nabla \psi_{D_{n_k}} \nabla \phi dx - \int_{\Gamma} g \phi d\sigma = 0, \forall \phi \in V(\tilde{U}), \quad (\text{C12})$$

$$\begin{aligned} \text{find } \psi_{R_{n_k}} \in H^1(\Omega_{n_k}), \text{ such that: } & \int_{\Omega_{n_k}} \nabla \psi_{R_{n_k}} \nabla \phi dx + \beta \int_{\Sigma_{n_k}} \psi_{R_{n_k}} \phi d\sigma - \int_{\Sigma_{n_k}} h \phi d\sigma \\ & - \int_{\Gamma} g \phi d\sigma = 0, \forall \phi \in H^1(\tilde{U}). \end{aligned} \quad (\text{C13})$$

Now we prove the convergence of the sequences $\psi_{D_{n_k}} \rightarrow \psi_D$ in $V(\tilde{U})$ and $\psi_{R_{n_k}} \rightarrow \psi_R$ in $H^1(\tilde{U})$.

For $\psi_{R_{n_k}}$, we analyze its boundedness via the elliptic property of the governing equations. A standard technique is to select the test function $\phi = \psi_{R_{n_k}}$, enabling estimation of the upper bound in the $H^1(\Omega_{n_k})$ norm through the following equation

$$\int_{\Omega_{n_k}} \nabla \psi_{R_{n_k}} \nabla \psi_{R_{n_k}} dx + \beta \int_{\Sigma_{n_k}} \psi_{R_{n_k}} \cdot \psi_{R_{n_k}} d\sigma - \int_{\Sigma_{n_k}} h \psi_{R_{n_k}} d\sigma - \int_{\Gamma} g \psi_{R_{n_k}} d\sigma = 0. \quad (\text{C14})$$

The $H^1(\Omega_{n_k})$ -norm is defined by equation (2). Using the elliptic property, we derive the estimate $\exists \alpha_k > 0$, such that

$$\int_{\Omega_{n_k}} \nabla \psi_{R_{n_k}} \nabla \psi_{R_{n_k}} dx + \beta \int_{\Sigma_{n_k}} \psi_{R_{n_k}} \cdot \psi_{R_{n_k}} d\sigma \geq \alpha_k \|\psi_{R_{n_k}}\|_{H^1(\Omega_{n_k})}^2, \quad (\text{C15})$$

We apply the Cauchy Schwarz inequality to estimate the boundary integrals

$$\left| \int_{\Sigma_{n_k}} h \psi_{R_{n_k}} d\sigma + \int_{\Gamma} g \psi_{R_{n_k}} d\sigma \right| \leq |\tilde{U}|^{\frac{1}{2}} \left(\|\psi_{R_{n_k}}\|_{L^2(\Sigma_{n_k})} \max_{\Sigma_{n_k}} |h| + \|\psi_{R_{n_k}}\|_{L^2(\Gamma)} \max_{\Gamma} |g| \right), \quad (\text{C16})$$

where $|\tilde{U}|$ is the maximum diameter of the domain \tilde{U} . The compactness of the boundaries Σ_{n_k} and Γ ensures the existence of this maximum. Combining equations (C15) and (C16), we obtain

$$\begin{aligned} \alpha_k \|\psi_{R_{n_k}}\|_{H^1(\Omega_{n_k})}^2 & \leq |\tilde{U}|^{\frac{1}{2}} \left(\|\psi_{R_{n_k}}\|_{L^2(\Sigma_{n_k})} \max_{\Sigma_{n_k}} |h| + \|\psi_{R_{n_k}}\|_{L^2(\Gamma)} \max_{\Gamma} |g| \right) \\ & \leq \tilde{C} \left(\|\psi_{R_{n_k}}\|_{L^2(\Sigma_{n_k})} + \|\psi_{R_{n_k}}\|_{L^2(\Gamma)} \right), \end{aligned} \quad (\text{C17})$$

where $\tilde{C} = \max\{|\tilde{U}|^{\frac{1}{2}} \max_{\Sigma_{n_k}} |h|, |\tilde{U}|^{\frac{1}{2}} \max_{\Gamma} |g|\}$ and the right hand side of inequality (C17) can be further raised using the trace theorem:

$$\begin{aligned} \|\psi_{R_{n_k}}\|_{L^2(\Sigma_{n_k})} & \leq C_1 \|\psi_{R_{n_k}}\|_{H^1(\Omega_{n_k})} \leq \tilde{C}_1 \|\psi_{R_{n_k}}\|_{H^1(\tilde{U})}, \\ \|\psi_{R_{n_k}}\|_{L^2(\Gamma)} & \leq C_2 \|\psi_{R_{n_k}}\|_{H^1(\Omega_{n_k})} \leq \tilde{C}_2 \|\psi_{R_{n_k}}\|_{H^1(\tilde{U})}, \end{aligned} \quad (\text{C18})$$

Then, the norm is formulated by the domain extension with the constants E_1, E_2 to derive the following equivalent theorem:

$$E_1 \|\psi\|_{H^1(\tilde{U})} \leq \|\psi\|_{H^1(\Omega_{n_k})} \leq E_2 \|\psi\|_{H^1(\tilde{U})}. \quad (\text{C19})$$

By the formula (C17), (C18) and (C19), we conclude the sequence ψ_{n_k} is bounded.

$$\begin{aligned} \alpha_k \|\psi\|_{H^1(\Omega_{n_k})}^2 &\leq \tilde{C} \left(\|\psi_{R_{n_k}}\|_{L^2(\Sigma_{n_k})} + \|\psi_{R_{n_k}}\|_{L^2(\Gamma)} \right) \\ &\leq \tilde{C} \max\{\tilde{C}_1, \tilde{C}_2\} \|\psi_{n_k}\|_{H^1(\tilde{U})} \\ &\leq \tilde{C} \max\{\tilde{C}_1, \tilde{C}_2\} E_1^{-1} \|\psi\|_{H^1(\Omega_{n_k})}, \end{aligned} \quad (\text{C20})$$

where we denote the extension factor by $c = (\tilde{C} \max\{\tilde{C}_1, \tilde{C}_2\}) \cdot (E_1 \alpha_k)^{-1}$. Then, the boundedness of sequence $\{\psi_{n_k}\}$ is proven:

$$\|\psi_{n_k}\|_{H^1(\tilde{U})} \leq c \cdot E_1. \quad (\text{C21})$$

Hence, there exists a unique limit point ψ_R for this bounded convergent sequence in $H^1(\tilde{U})$. The above proof applies analogously to the convergence $\psi_{D_{n_k}} \rightarrow \psi_D$ in $V(\tilde{U})$. Next, we verify that the limit points ψ_D and ψ_R satisfy the variational equations (C12) and (C13) in the domain $\Omega(\Sigma(\varphi))$, respectively.

Considering the $\psi_R(\varphi) = \psi_R|_{\Omega(\Sigma(\varphi))}$, the variational equation (C13) can be expressed as

$$\int_{\Omega(\Sigma(\varphi))} \nabla \psi_R \nabla \phi dx + \beta \int_{\Sigma(\varphi)} \psi_R \phi d\sigma - \int_{\Sigma(\varphi)} h \phi d\sigma - \int_{\Gamma} g \phi d\sigma = 0, \quad (\text{C22})$$

where ϕ is the test function in $H^1(\Omega(\Sigma(\varphi)))$.

For the subsequence ψ_{n_k} of the solution to Eq.(C13), the variational equation is

$$\int_{\Omega_{n_k}} \nabla \psi_{R_{n_k}} \nabla \phi dx + \beta \int_{\Sigma_{n_k}} \psi_{R_{n_k}} \phi d\sigma - \int_{\Sigma_{n_k}} h \phi d\sigma - \int_{\Gamma} g \phi d\sigma = 0. \quad (\text{C23})$$

We consider the difference between (C22) and (C23), where the test function ϕ in $H^1(\tilde{U})$ is limited to $H^1(\Omega(\Sigma(\varphi)))$. Taking the limit $k \rightarrow \infty$, the difference of two variational equations can be formulated as follows:

$$\begin{aligned} D_1 &= \left| \int_{\Omega(\Sigma(\varphi))} \nabla \psi_R \nabla \phi dx - \int_{\Omega_{n_k}} \nabla \psi_{R_{n_k}} \nabla \phi dx \right|, \\ D_2 &= \beta \left| \int_{\Sigma(\varphi)} \psi_R \phi d\sigma - \int_{\Sigma_{n_k}} \psi_{R_{n_k}} \phi d\sigma \right|, \\ D_3 &= \left| \int_{\Sigma(\varphi)} h \phi d\sigma - \int_{\Sigma_{n_k}} h \phi d\sigma \right|, \\ D_4 &= \left| \int_{\Gamma} g \phi d\sigma - \int_{\Gamma} g \phi d\sigma \right|, \end{aligned} \quad (\text{C24})$$

where D_4 is independent of the index k , hence $D_4 = 0$.

Considering the difference D_1 , we extend the integral over the domain \tilde{U} using the characteristic function ζ

$$\begin{aligned}
 D_1 &= \left| \int_{\Omega(\Sigma(\varphi))} \nabla \psi_R \nabla \phi dx - \int_{\Omega_{n_k}} \nabla \psi_{R_{n_k}} \nabla \phi dx \right| \\
 &= \left| \int_{\tilde{U}} \zeta_{\Omega(\varphi)} \nabla \tilde{\psi}_R \nabla \phi dx - \int_{\tilde{U}} \zeta_{\Omega_k} \nabla \tilde{\psi}_{R_{n_k}} \nabla \phi dx \right| \\
 &= \left| \int_{\tilde{U}} \zeta_{\Omega(\varphi)} (\nabla \tilde{\psi}_R - \nabla \tilde{\psi}_{R_{n_k}}) \nabla \phi dx + \int_{\tilde{U}} (\zeta_{\Omega(\varphi)} - \zeta_{\Omega_k}) \nabla \tilde{\psi}_{R_{n_k}} \nabla \phi dx \right| \\
 &\leq \left| \int_{\tilde{U}} \zeta_{\Omega(\varphi)} (\nabla \tilde{\psi}_R - \nabla \tilde{\psi}_{R_{n_k}}) \nabla \phi dx \right| + \left| \int_{\tilde{U}} (\zeta_{\Omega(\varphi)} - \zeta_{\Omega_k}) \nabla \tilde{\psi}_{R_{n_k}} \nabla \phi dx \right|,
 \end{aligned} \tag{C25}$$

where $\tilde{\psi}_R, \tilde{\psi}_{R_{n_k}}$ are the zero extensions of $\psi_R, \psi_{R_{n_k}}$ in \tilde{U} , respectively. As $k \rightarrow \infty$, the first term on the right hand side converges to zero, as demonstrated by the convergence of the sequence ψ_{n_k} in $H^1(\tilde{U})$. The convergence of the characteristic functions ζ_k corresponds the convergence of the domain sequence parameterized by φ_{n_k} for the second term.

Considering the difference D_2 , we first perform a parameter transformation using y along the boundary Σ and estimate the upper bound via triangle inequality:

$$\begin{aligned}
 D_2 &= \beta \left| \int_{\Sigma(\varphi)} \psi_R \phi d\sigma - \int_{\Sigma_{n_k}} \psi_{R_{n_k}} \phi d\sigma \right| \\
 &= \beta \left| \int_{\mathbb{S}^2} (\psi_R \circ \varphi(y)) (\phi \circ \varphi(y)) J_\varphi(y) - (\psi_{R_{n_k}} \circ \varphi_{n_k}(y)) (\phi \circ \varphi_{n_k}(y)) J_{\varphi_k}(y) d\sigma(y) \right| \\
 &\leq \beta \left| \int_{\mathbb{S}^2} (\psi_R \circ \varphi) (\phi \circ \varphi) (J_\varphi - J_{\varphi_k}) d\sigma \right| + \beta \left| \int_{\mathbb{S}^2} (\psi_R \circ \varphi) (\phi \circ \varphi - \phi \circ \varphi_{n_k}) J_{\varphi_k} d\sigma \right| \\
 &\quad + \beta \left| \int_{\mathbb{S}^2} (\psi_R \circ \varphi - \psi_{R_{n_k}} \circ \varphi) (\phi \circ \varphi_{n_k}) J_{\varphi_k} d\sigma \right| \\
 &\quad + \beta \left| \int_{\mathbb{S}^2} (\psi_{R_{n_k}} \circ \varphi - \psi_{R_{n_k}} \circ \varphi_{R_{n_k}}) (\phi \circ \varphi_{n_k}) J_{\varphi_k} d\sigma \right|,
 \end{aligned} \tag{C26}$$

where J_φ is the Jacobian of parameter transformation represented by $\varphi = r(y)y$, $y \in \mathbb{S}^2$, then $J_\varphi = r \cdot (r^2 + \nabla r \cdot \nabla r)^{\frac{1}{2}}$. For $\forall \varphi \in \mathcal{P}$, there exist positive constants c_1, c_2 such that $c_1 \leq |\det(J_\varphi)| \leq c_2$. Next, we estimate each term on the right side hand using the

Cauchy Schwarz inequality:

$$\begin{aligned}
 \text{term 1} &= \beta \left| \int_{\mathbb{S}^2} (\psi_R \circ \varphi) (\phi \circ \varphi) (J_\varphi - J_{\varphi_k}) d\sigma \right| \\
 &= \beta \left| \int_{\mathbb{S}^2} (\psi_R \circ \varphi) (\phi \circ \varphi) J_\varphi \frac{(J_\varphi - J_{\varphi_k})}{J_\varphi} d\sigma \right| \\
 &\leq \beta \sup_{\mathbb{S}^2} |J_\varphi - J_{\varphi_k}| \cdot c_1^{-1} \left| \int_{\mathbb{S}^2} (\psi_R \circ \varphi) (\phi \circ \varphi) J_\varphi d\sigma \right| \\
 &\leq \beta \sup_{\mathbb{S}^2} |J_\varphi - J_{\varphi_k}| \cdot c_1^{-1} \|\psi_R\|_{L^2(\Sigma(\varphi))} \|\phi\|_{L^2(\Sigma(\varphi))}, \\
 \text{term 2} &= \beta \left| \int_{\mathbb{S}^2} (\psi_R \circ \varphi) (\phi \circ \varphi - \phi \circ \varphi_{n_k}) J_{\varphi_k} d\sigma \right| \\
 &= \beta \left| \int_{\mathbb{S}^2} (\psi_R \circ \varphi) (\phi \circ \varphi - \phi \circ \varphi_{n_k}) J_{\varphi_k} \cdot \sqrt{\frac{J_\varphi}{J_{\varphi_k}}} d\sigma \right| \\
 &\leq \beta \left| \int_{\mathbb{S}^2} (\psi_R \circ \varphi)^2 J_{\varphi_k}^2 \cdot \frac{J_\varphi}{J_{\varphi_k}} d\sigma \right|^{\frac{1}{2}} \cdot \|(\phi \circ \varphi - \phi \circ \varphi_{n_k})\|_{L^2(\mathbb{S}^2)} \\
 &\leq \beta c_2 \cdot c_1^{-\frac{1}{2}} \|\psi_R\|_{L^2(\Sigma(\varphi))} \|(\phi \circ \varphi - \phi \circ \varphi_{n_k})\|_{L^2(\mathbb{S}^2)}, \\
 \text{term 3} &= \beta \left| \int_{\mathbb{S}^2} (\psi_R \circ \varphi - \psi_{R_{n_k}} \circ \varphi) (\phi \circ \varphi_{n_k}) J_{\varphi_k} d\sigma \right| \\
 &\leq \beta c_2^{\frac{1}{2}} \cdot c_1^{-\frac{1}{2}} \|\psi_R - \psi_{R_{n_k}}\|_{L^2(\Sigma(\varphi))} \|\phi\|_{L^2(\Sigma_k)}, \\
 \text{term 4} &= \beta \left| \int_{\mathbb{S}^2} (\psi_{R_{n_k}} \circ \varphi - \psi_{R_{n_k}} \circ \varphi_{R_{n_k}}) (\phi \circ \varphi_{n_k}) J_{\varphi_k} d\sigma \right| \\
 &\leq \beta c_2^{\frac{1}{2}} \|\psi_{R_{n_k}} \circ \varphi - \psi_{R_{n_k}} \circ \varphi_{R_{n_k}}\|_{L^2(\mathbb{S}^2)} \|\phi\|_{L^2(\Sigma_k)},
 \end{aligned} \tag{C27}$$

where $\forall \varphi \in \mathcal{P}$, $J_\varphi \neq 0$ by the definition of a regular parameter transformation. The convergence of each term is evident from the sequences J_{φ_k} and $\psi_{R_{n_k}}$ in $H^1(\tilde{U})$. Hence, D_2 converges to 0 as $k \rightarrow \infty$.

Considering the difference D_3 , we apply the same parameter transformation method.

$$\begin{aligned}
 D_3 &= \left| \int_{\Sigma(\varphi)} h\phi d\sigma - \int_{\Sigma_{n_k}} h\phi d\sigma \right|, \\
 &= \left| \int_{\mathbb{S}^2} (h \circ \varphi) (\phi \circ \varphi) J_\varphi d\sigma - \int_{\mathbb{S}^2} (h \circ \varphi_{n_k}) (\phi \circ \varphi_{n_k}) J_{\varphi_k} d\sigma \right|, \\
 &\leq \left| \int_{\mathbb{S}^2} (h \circ \varphi) (\phi \circ \varphi) (J_\varphi - J_{\varphi_k}) d\sigma \right| + \left| \int_{\mathbb{S}^2} (h \circ \varphi - h \circ \varphi_{n_k}) (\phi \circ \varphi) J_{\varphi_k} d\sigma \right| \\
 &\quad + \left| \int_{\mathbb{S}^2} (h \circ \varphi_{n_k}) (\phi \circ \varphi - \phi \circ \varphi_{n_k}) J_{\varphi_k} d\sigma \right| + \left| \int_{\mathbb{S}^2} (h \circ \varphi_{n_k}) (\phi \circ \varphi_{n_k} - \phi \circ \varphi_{n_k}) J_{\varphi_k} d\sigma \right|,
 \end{aligned} \tag{C28}$$

where the last term on the right hand side is equal to 0. As in the analysis of D_2 , we infer that D_3 converges to 0 as $k \rightarrow \infty$. The convergence of sequence ψ_D is proven in the same way.

Hence, equation (C23) converges to the equation (C22) as $k \rightarrow \infty$. This proves the compactness of set \mathcal{M} in $\mathcal{P} \times V(\tilde{U}) \times H^1(\tilde{U})$. \square